

Cytoplasmic condensation induced by membrane damage is associated with antibiotic lethality

Felix Wong ^{1,2}, Jonathan M. Stokes^{1,2}, Bernardo Cervantes^{1,2,3}, Sider Penkov⁴, Jens Friedrichs⁵, Lars D. Renner ⁵✉ & James J. Collins ^{1,2,6}✉

Bactericidal antibiotics kill bacteria by perturbing various cellular targets and processes. Disruption of the primary antibiotic-binding partner induces a cascade of molecular events, leading to overproduction of reactive metabolic by-products. It remains unclear, however, how these molecular events contribute to bacterial cell death. Here, we take a single-cell physical biology approach to probe antibiotic function. We show that aminoglycosides and fluoroquinolones induce cytoplasmic condensation through membrane damage and subsequent outflow of cytoplasmic contents as part of their lethality. A quantitative model of membrane damage and cytoplasmic leakage indicates that a small number of nanometer-scale membrane defects in a single bacterium can give rise to the cellular-scale phenotype of cytoplasmic condensation. Furthermore, cytoplasmic condensation is associated with the accumulation of reactive metabolic by-products and lipid peroxidation, and pretreatment of cells with the antioxidant glutathione attenuates cytoplasmic condensation and cell death. Our work expands our understanding of the downstream molecular events that are associated with antibiotic lethality, revealing cytoplasmic condensation as a phenotypic feature of antibiotic-induced bacterial cell death.

¹Institute for Medical Engineering & Science and Department of Biological Engineering, Massachusetts Institute of Technology, Cambridge, MA, USA.

²Infectious Disease and Microbiome Program, Broad Institute of MIT and Harvard, Cambridge, MA, USA. ³Microbiology Graduate Program, Massachusetts Institute of Technology, Cambridge, MA, USA. ⁴Institute for Clinical Chemistry and Laboratory Medicine at the University Clinic and Medical Faculty of TU Dresden, Dresden, Germany. ⁵Leibniz Institute of Polymer Research and the Max Bergmann Center of Biomaterials, Dresden, Germany. ⁶Wyss Institute for Biologically Inspired Engineering, Harvard University, Boston, MA, USA. ✉email: renner@ipfdd.de; jimjc@mit.edu

Understanding the detailed mechanisms of action of antibiotics remains a central focus in microbiology¹. While the primary binding partners of antibiotics have been largely classified, we still lack a holistic understanding of how bactericidal antibiotics lead to cell death². Such an understanding would better inform the use and misuse of antibiotics, in addition to approaches for addressing antibiotic resistance.

Previous work has shown that the intracellular accumulation of promiscuously reactive metabolic by-products induces widespread cellular dysfunction and contributes to antibiotic lethality^{2–13}. However, the mechanisms underlying how reactive metabolic by-products, and the accompanying phenotypic changes, contribute to cell death have remained unclear. In contrast to conventional approaches that study bacterial responses to antibiotics in bulk culture, we reasoned that analyses of single cells through a physical biology approach^{14–16} could allow for a more nuanced understanding of how cell death occurs downstream of the primary drug–target interaction. To this end, we investigated in *Escherichia coli* the single-cell response to three main classes of bactericidal antibiotics: aminoglycosides, which corrupt mRNA proofreading by the 30S ribosomal subunit; fluoroquinolones, which perturb DNA replication; and β -lactams, which disrupt peptidoglycan cell wall biosynthesis through perturbation of penicillin-binding proteins. Here, we show that, in contrast to the lytic mode of action of β -lactams, aminoglycosides and fluoroquinolones induce a phenotype of cytoplasmic condensation through membrane damage. This phenotype is associated with the accumulation of reactive metabolic by-products, lipid peroxidation, and cell death, thus indicating a sequence of cellular events through which reactive metabolic products can lead to antibiotic-induced cell death.

Results

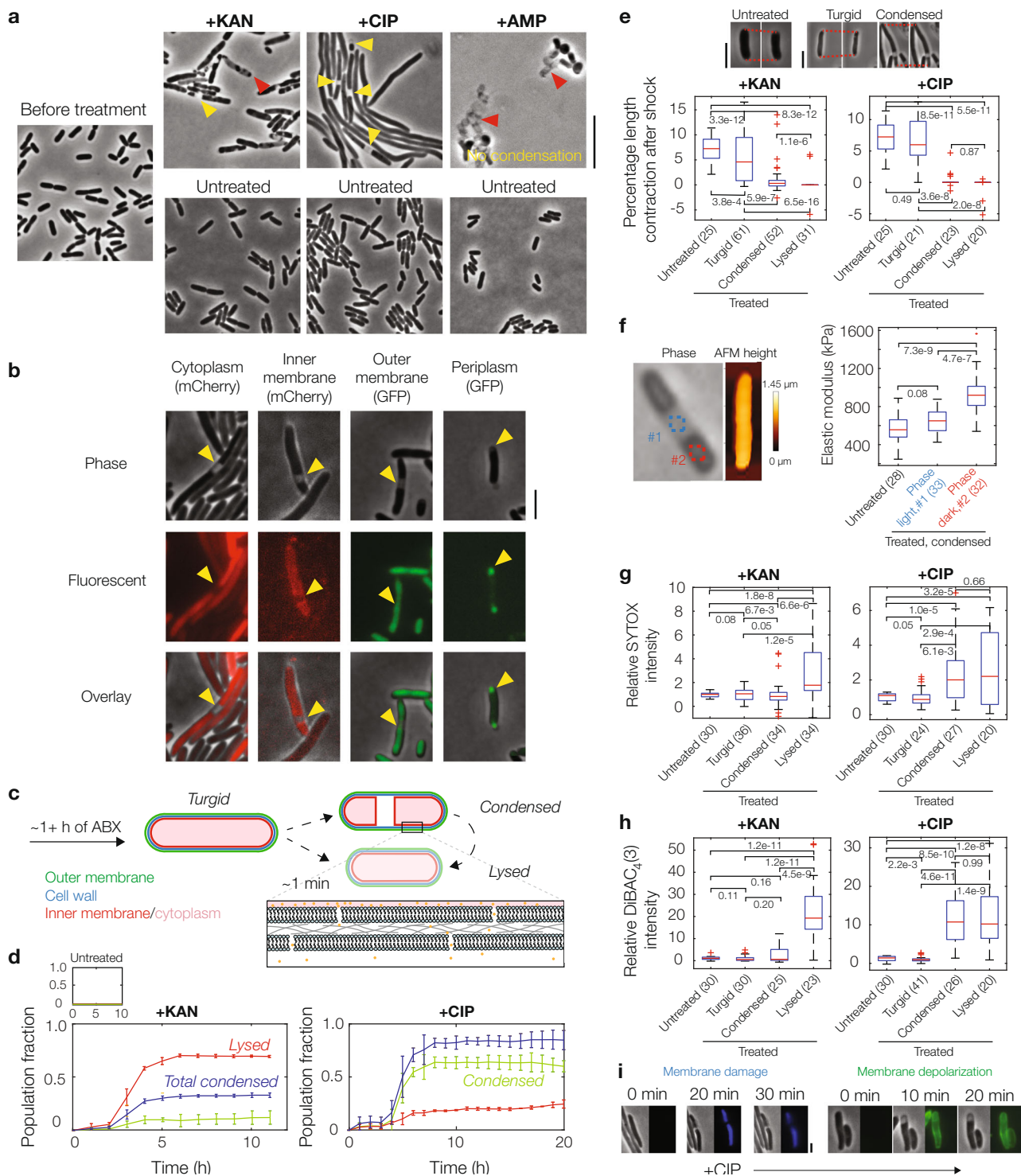
Aminoglycosides and fluoroquinolones induce membrane damage and cytoplasmic condensation in *E. coli*. To probe how aminoglycoside, fluoroquinolone, and β -lactam antibiotics kill metabolically active bacterial cells, we treated log-phase *E. coli* with the aminoglycoside kanamycin, the fluoroquinolone ciprofloxacin, and the β -lactam ampicillin at various concentrations ranging from 1 \times to 100 \times the minimum inhibitory concentration (MIC; Supplementary Table 1). Using long-term microfluidic imaging across these conditions, we observed variability in the morphological dynamics of cells, which, aside from filamentation, could be characterized by three modes: cytoplasmic condensation, membrane bulging, and lysis (Fig. 1a and Supplementary Movies 1–3). Interestingly, some cells treated with kanamycin and most cells treated with ciprofloxacin, but no cells treated with ampicillin, exhibited cytoplasmic condensation, a phenotype in which the cytoplasm fragments and grows denser, as manifested by the appearance of discrete, phase-light regions between phase-dark regions that grow darker (Supplementary Figs. 1 and 2, and Supplementary Note 1). Since previous work has explored how β -lactam-mediated perturbation of peptidoglycan biosynthesis leads to membrane bulging and lysis¹⁷, we ventured to explore further in this work the condensation phenotype induced by aminoglycosides and fluoroquinolones.

In cells that have exhibited cytoplasmic condensation, which comprised ~30% of cells treated with kanamycin and ~90% of cells treated with ciprofloxacin, as distinguished visually from long-term timelapses (Fig. 1d), discrete portions of cells typically became phase-light over a timescale of ~1 min. This phenotype characteristically appeared after tens of minutes, or hours, after antibiotic exposure (Fig. 1d), with larger antibiotic concentrations typically resulting in earlier condensation (Supplementary Movies 2 and 3). Subsequent imaging with fluorescent tags

labeling the inner membrane, outer membrane, cytoplasm, and periplasm revealed that the cytoplasm of these cells was plasmolyzed: the inner membrane was retracted from the outer membrane and the periplasmic space corresponding to phase-light regions was increased (Fig. 1b, c), similar to osmotically shocked cells¹⁸. Supporting the notion that the cytoplasmic contents of these cells are compactified, fluorescence microscopy measurements with a strain exhibiting cytoplasmic fluorescence indicated increased fluorescence intensities in condensed, phase-dark regions (Supplementary Fig. 2). Minutes to hours after the occurrence of condensation, most condensed cells (~90%) eventually lysed (Fig. 1d), as determined by the cytoplasm becoming entirely phase-light. Emphasizing the generality of these phenotypes, we found that cytoplasmic condensation and lysis were shared among different aminoglycosides and fluoroquinolones (Supplementary Fig. 3) and across different antibiotic concentrations (Supplementary Fig. 4), as well as in the Gram-positive bacterium *Bacillus subtilis* during antibiotic treatment, for which we observed that the cytoplasm appeared to retract from the cell wall (Supplementary Fig. 3).

Cytoplasmic condensation and lysis typically require loss of cellular turgor or membrane integrity¹⁷, which are distinct from the primary mechanisms of action of aminoglycosides and fluoroquinolones. Indeed, under standard laboratory conditions, *E. coli* maintains a turgor pressure of ~1 atm which presses its inner membrane against the cell wall¹⁹, raising the question of how condensation of the cytoplasm could physically occur. We hypothesized that the observed condensation and lysis were caused by loss of turgor. To test this hypothesis, we independently: (i) osmotically shocked the cells using flow of hyperosmotic media (Fig. 1e and Supplementary Fig. 5); and (ii) probed the concentration of potassium, an intracellular solute, using a membrane-permeable potassium-sensitive dye, ION Potassium Green (IPG; Supplementary Fig. 6). Quantifying the cellular response to a 500 mM hyperosmotic shock—corresponding to approximately ten times *E. coli*'s estimated turgor pressure¹⁹—revealed that condensed and lysed cells exhibited smaller length contractions compared to turgid ones (Fig. 1e and Supplementary Fig. 5). As the cell envelopes of cells with larger turgor pressures are more stretched¹⁷, this observation indicates that the turgor of condensed and lysed cells was significantly diminished compared to turgid cells, and that cytoplasmic condensation could occur through loss of cellular turgor (Supplementary Note 1). These observations are consistent with measurements of IPG fluorescence, which we found to be decreased in condensed cells (Supplementary Fig. 6), suggesting that the loss of cellular turgor is associated with the depletion of intracellular solutes including potassium ions.

To better understand how the mechanical properties of cells change during condensation, we next quantified the effective elastic moduli of cells using atomic force microscopy (AFM; Fig. 1f and Supplementary Fig. 7). AFM experiments on condensed, antibiotic-treated cells revealed that, in ciprofloxacin-treated cells, the phase-dark regions of condensed cells exhibit significantly larger elastic moduli than corresponding regions in turgid cells, which, in turn, exhibit similar elastic moduli to phase-light regions (Fig. 1f and Supplementary Fig. 7). As *E. coli*'s turgor pressure has been estimated to be ~1 atm¹⁹, consistent with inferred values based on our AFM measurements (see Methods for details), these observations suggest that decreases in effective stiffness, arising from the loss of turgor pressure during cytoplasmic condensation, may be offset by the intracellular compactification of macromolecules suggested by phase-contrast and fluorescence microscopy measurements (Supplementary Fig. 2). Intriguingly, we observed similar, but less pronounced, variations in cell stiffness in kanamycin-treated cells, whose cell-



averaged elastic moduli are not significantly changed relative to those of untreated cells (Supplementary Fig. 7). It is possible that this difference between condensed ciprofloxacin- and kanamycin-treated cells could arise from additional membrane damage through ribosome-independent ionic interactions of aminoglycosides with the outer membrane, which contributes to destabilizing the cellular envelope²⁰. Another possibility suggested by our fluorescence intensity measurements (Supplementary Fig. 2) is that, while cellular turgor is decreased in condensed cells treated with either antibiotic, less intracellular compactification of macromolecules occurs in kanamycin-treated cells. Thus, these

AFM experiments suggest that cytoplasmic condensation affects the effective elastic moduli of antibiotic-treated cells to varying degrees.

We next investigated whether the observed loss of turgor arose specifically from membrane damage, resulting in the outflow of cytoplasmic contents. Addition of SYTOX Blue, a DNA intercalating dye that only penetrates cells with compromised membranes, to drug-treated cells indicated loss of membrane integrity in condensed and lysed cells, with kanamycin-treated cells exhibiting significant increases in fluorescence at lysis and ciprofloxacin-treated cells exhibiting significant increases in

Fig. 1 Aminoglycoside and fluoroquinolone antibiotics induce cytoplasmic condensation in *E. coli*. **a** Cytoplasmic condensation and/or lysis (yellow and red markers, respectively) induced by kanamycin (KAN), ciprofloxacin (CIP), and ampicillin (AMP) after 1–6 h of treatment (KAN: 3 h, CIP: 6 h, AMP: 1 h) in a population of wild-type, log-phase *Escherichia coli* cells, imaged in phase contrast. Times were chosen to reflect timescales of phenotypic change. Here and below, all antibiotic concentrations used were 10× MIC, while control cells were untreated; working MICs were 5 µg/mL for kanamycin, 0.1 µg/mL for ciprofloxacin, and 10 µg/mL for ampicillin. Ampicillin-treated cells exhibited membrane bulging and lysis, in contrast to cytoplasmic condensation and lysis observed in kanamycin- and ciprofloxacin-treated cells (Supplementary Fig. 1). Ciprofloxacin-treated cells also displayed filamentation. Cytoplasmic condensation and lysis were general across cells in a population, antibiotic concentrations ranging at least from 1× to 100× MIC, different aminoglycoside and fluoroquinolone antibiotics, and in *Bacillus subtilis* (Supplementary Figs. 3 and 4). Results are representative of three biological replicates in each condition. Scale bar, 10 µm. **b** *E. coli* cells with fluorescent genetic outer membrane (green fluorescent protein, GFP), inner membrane (mCherry), periplasmic (GFP), and cytoplasmic (mCherry) markers under ciprofloxacin treatment, imaged in phase contrast and epifluorescence. For similar cells treated with kanamycin, see Supplementary Fig. 3. Results are representative of three biological replicates for each marker, and yellow markers highlight condensed cells. Scale bars here and below, 3 µm. **c** Schematic of cytoplasmic condensation and lysis in *E. coli* treated with kanamycin and ciprofloxacin. **d** Fractions of all cells that are condensed or lysed. Error bars indicate one standard deviation, and data are presented as mean ± SEM. Data are derived from two different fields of view with at least 100 cells each (kanamycin, 133 and 149 cells; ciprofloxacin, 255 and 140 cells) and representative of two biological replicates. Note that cells may condense and lyse within the same hour; such cells are reflected only in lysed cell counts. The total condensed fraction counts all cells that are, or have previously been, condensed. **e** Hyperosmotic shock measurements in control and antibiotic-treated *E. coli*, of which three characteristic phase-contrast microscopy images are shown (top); here, ciprofloxacin-treated cells are shown. The percentage length contraction, an indicator of cellular turgor, is the percentage change in cell length immediately after hyperosmotic shock. Red dashed lines represent visual guides. The number of cells in each group are indicated in parentheses. Here and below, a box plot indicating the median (center), 25th and 75th percentile (bounds of box), and extreme data points not considered outliers (bounds of whiskers) is shown, and red crosses indicate outliers including the minimum and maximum values. *p*-values for two-sample Kolmogorov-Smirnov tests are shown next to corresponding brackets. **f** Atomic force microscopy (AFM) of cells. (Left) Phase-contrast and AFM topography image of a condensed, ciprofloxacin-treated cell. (Right) Inferred elastic moduli corresponding to the cellular regions shown to the left, as indicated by different colors, as well as along the cellular body of an untreated control cell. The number of cells in each group are indicated in parentheses. Box plot features and statistical tests refer to those of panel (e). For measurements for kanamycin-treated cells, see Supplementary Fig. 7. **g, h** Fluorescence intensities of control and antibiotic-treated *E. coli* in the presence of SYTOX Blue (g) and DiBAC₄(3) (h). The number of cells in each group are indicated in parentheses. Box plot features and statistical tests refer to those of panel (e). **i** Representative timelapses of ciprofloxacin-treated *E. coli* stained by SYTOX Blue and DiBAC₄(3), imaged in phase contrast and epifluorescence. Times show duration after the first image, and results are representative of three biological replicates.

fluorescence during condensation (Fig. 1g, i and Supplementary Fig. 8); we speculate that this difference may arise from varying levels of membrane damage, as well as earlier lysis after condensation in kanamycin-treated cells (Supplementary Fig. 9), which might allow for limited intercalation of dyes in these cells before lysis. Application of the membrane potential-sensitive dye DiBAC₄(3) similarly indicated membrane depolarization concomitant with membrane damage (Fig. 1h, i and Supplementary Fig. 8). Consistently, as a control, fluorescence of SYTOX Blue and DiBAC₄(3) did not occur for plasmolyzed cells that were subjected to a 500 mM hyperosmotic shock, for which no cells lysed (Supplementary Fig. 8). Taken together, these results reveal that aminoglycosides and fluoroquinolones can induce cytoplasmic condensation and lysis through membrane damage, and, as suggested by SYTOX Blue, this membrane damage coincides with loss of cell viability. As detailed below, further time-kill assays confirm that the observed membrane damage accompanies loss of cell viability.

A biophysical model of cell envelope mechanics and solute outflow predicts the dynamics of cytoplasmic condensation.

Having determined that cytoplasmic condensation occurs through antibiotic-induced membrane damage, we sought to better understand the extent of membrane damage and the physiology of condensed cells using biophysical modeling. To this end, building on previous work^{17,21,22}, we developed a model of cell envelope mechanics that predicts: (i) smaller turgor and cytoplasmic condensation to arise from the elastic relaxation to an equilibrium state, one which is governed by the outward flow of cytoplasmic solutes through nanometer-sized membrane defects; and (ii) the number of such defects consistent with the empirically observed ~1 min timescale and magnitude of cytoplasmic condensation (Fig. 2a–c, Supplementary Note 1, Supplementary Table 2, and Supplementary Fig. 10).

The model assumes, for simplicity, that a constant number of nanometer-scale defects are introduced into both the inner and outer membranes of a bacterium. These defects need not overlap across the cell envelope layers, and similar defects need not be introduced into the peptidoglycan cell wall because the cell wall is porous with characteristic pore areas of ~10 nm²²³. While similar membrane defects may be generated, and quickly alleviated, during processes including electroporation, the SYTOX Blue (Fig. 1g) and osmotic shock experiments (Fig. 1e) described above suggest that the membrane defects we consider are sustained across time, so that appreciable outflow of intracellular solutes and intercalation of fluorescent dyes occur. Based on a linear-elastic description of the cellular envelope and a simple model of fluid transport through Poiseuille flow, the model predicts that the hydrodynamic flow of solutes from the cytoplasm to the external milieu is laminar and results in a gradual loss of turgor (Fig. 2d, e). This loss of turgor decreases the mechanical strains in the cell envelope. In turn, solute outflow is attenuated because both the cellular turgor and the sizes of typical membrane nano-defects are decreased. Cytoplasmic condensation occurs as cell volume is lost (Fig. 2f and Supplementary Fig. 9), and the model predicts that condensation corresponds to a steady state of this dynamical system. Surprisingly, the model predicts that only 10 nanometer-scale defects, corresponding to loss of approximately 1 in 10⁶ of all membrane phospholipids, can quantitatively explain both the timescale and magnitude of cytoplasmic condensation (Fig. 2f). Thus, building on our empirical measurements, the model reveals that subtle changes to membrane integrity can provoke the cellular-scale phenotype of cytoplasmic condensation.

Cytoplasmic condensation is associated with cell death. To better understand the significance of membrane damage and accompanying cytoplasmic condensation in a more conventional experimental system, we performed single-cell analyses and

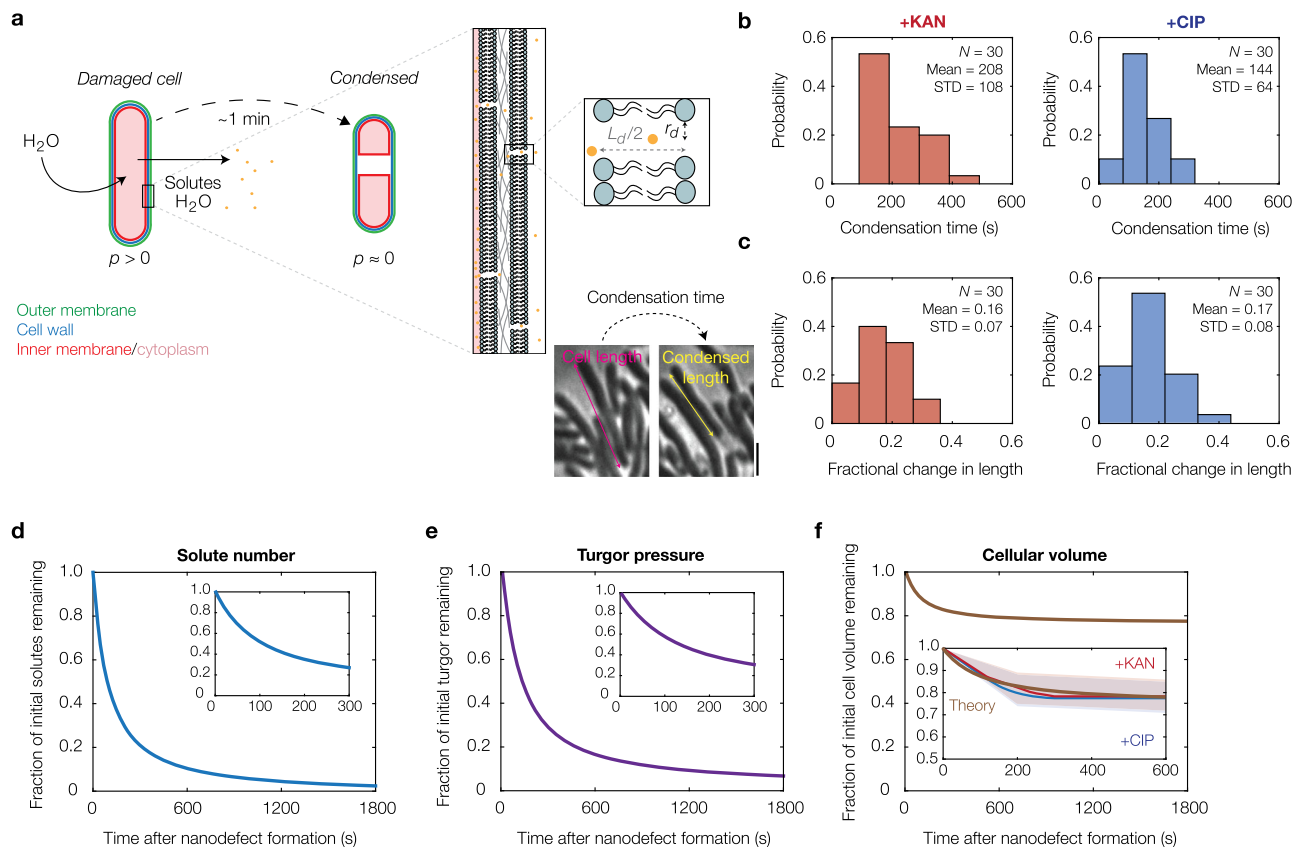


Fig. 2 Cytoplasmic condensation emerges from subtle, nanometer-scale membrane defects. **a** Model of condensation due to membrane nano-defect formation and subsequent solute leakage. Membrane nano-defects are modeled as circular channels that extrude through both the inner and outer membranes, with a typical radius of r_d and a typical length of L_d . Cytoplasmic condensation occurs as the cellular turgor (p) decreases. For details of the model, see Supplementary Note 1. **b** Empirically observed distributions of condensation times in kanamycin-treated and ciprofloxacin-treated cells at $10\times$ MIC. The cell numbers (N), population means, and standard deviations (STD) are indicated. **c** Same as panel (b) but for distributions of cell length changes, as illustrated in phase contrast for a typical ciprofloxacin-treated cell ($10\times$ MIC) in the inset (left; scale bar, $3\ \mu\text{m}$). **d-f** Model predictions for solute number (d), turgor pressure (e), and cell volume (f) against time after membrane nano-defect formation, for the characteristic parameter values summarized in Supplementary Table 2. (Insets) Plots for short times. The empirically observed decreases in cellular volume as functions of time for the kanamycin-treated and ciprofloxacin-treated ($10\times$ MIC) cells, represented in part by panels (b) and (c), are indicated by red and blue curves, respectively. Shaded regions indicate one standard deviation.

concurrent bulk time-kill assays. These revealed that condensation and lysis events occur in time concomitant with >1 log of killing in culture (Fig. 3a), as determined after plating and overnight incubation by colony-forming unit (CFU) quantification. We note here that decreases in CFUs were observed as soon as ~ 1 h after antibiotic treatment (Fig. 3a); however, this observation does not imply that cell death occurs before cytoplasmic condensation, since cell death may occur after plating in corresponding time-kill assays. Consistent with this hypothesis, recent work from the Zhao and Drlica labs has indicated that antibiotic-induced cell death occurs after plating on drug-free agar due, in part, to the post-stress accumulation of reactive oxygen species (ROS)¹¹, so that cell death may occur significantly after plating.

To further probe the notion that cells die on timescales longer than ~ 1 h of antibiotic treatment, we performed bacterial growth measurements at the single-cell level. These measurements showed that, in cells treated with ciprofloxacin, condensation represented an irreversible step at which cells failed to elongate and filament, with cessation of filamentation occurring at the time of condensation (Fig. 3b, c). Interestingly, kanamycin-treated cells exhibited increased growth variability before condensation and oscillatory cell length dynamics (Fig. 3d, e), consistent with repeated membrane swell–burst cycles²⁰ and

suggestive of more heterogeneous membrane damage compared to ciprofloxacin-treated cells. This observation is also consistent with earlier work showing that aminoglycosides induce outer membrane damage by ribosome-independent ionic interactions, which, along with subsequent membrane fusion, lead to repeated membrane swell–burst cycles²⁰. For both antibiotics, subsequent washout with drug-free growth media revealed that condensed and lysed cells do not recover from antibiotic treatment, while filamentous or dividing cells recover from antibiotic treatment and appear to proliferate (Fig. 3f, g and Supplementary Movies 4 and 5). These results indicate that the cessation of filamentation, seen in condensed cells, is associated with killing (Fig. 3b, c). Furthermore, these observations collectively suggest that cytoplasmic condensation is an irreversible phenotype distinguishing antibiotic susceptibility from tolerance, although we note here that, because antibiotic treatment leads to >1 log of killing but less than 90% of cells observed may be condensed, not all susceptible cells are condensed (Figs. 1d and 3a).

Unsurprisingly, experiments in which drug-tolerant stationary-phase cells were treated with kanamycin and ciprofloxacin revealed less killing in culture, and less cytoplasmic condensation and lysis in single cells (Supplementary Fig. 11). This is expected because recent work has shown that the lethality of different

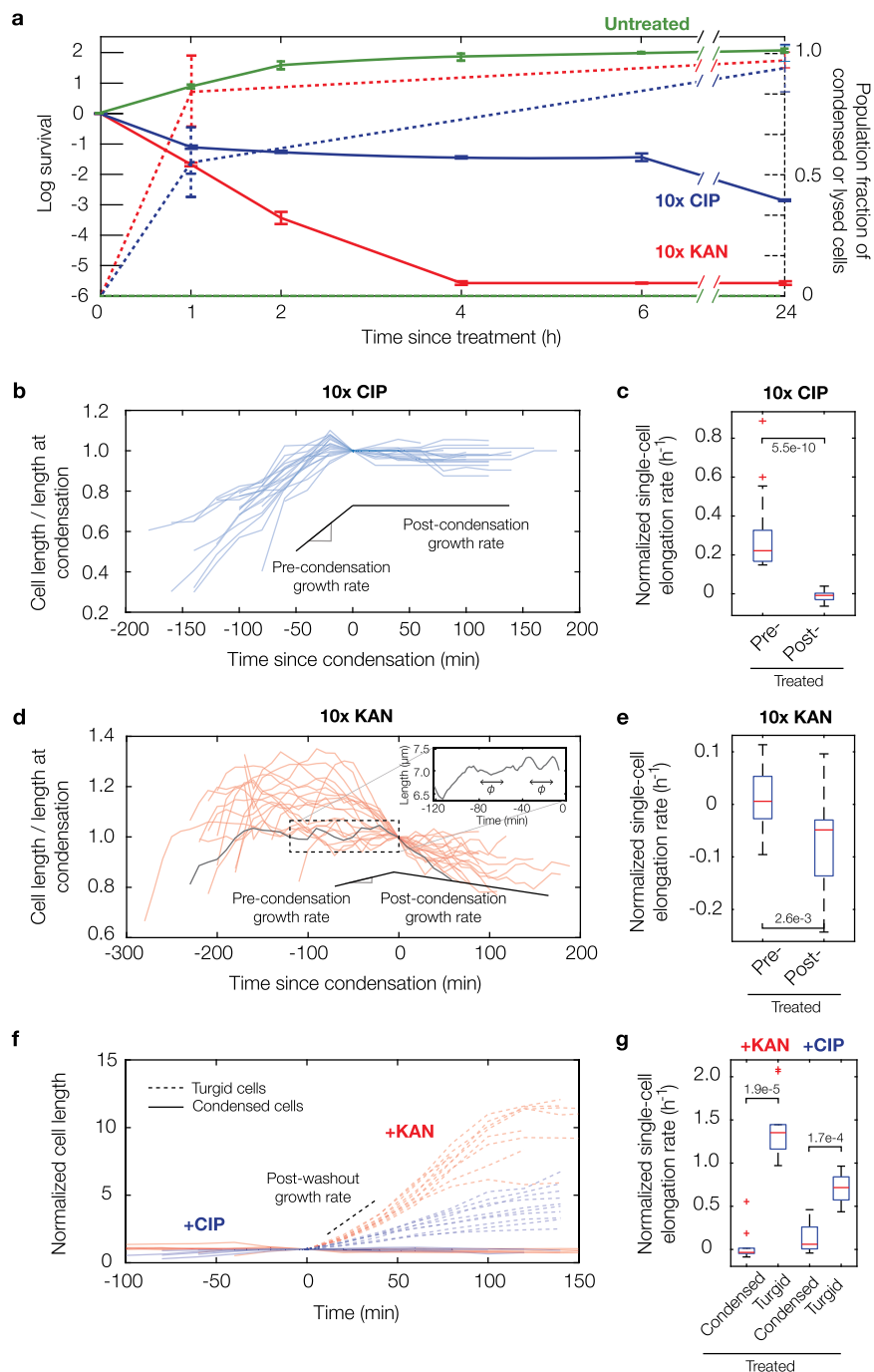


Fig. 3 Cytoplasmic condensation is an irreversible cell death phenotype. **a** Survival of log-phase bulk cultures of *E. coli* treated with kanamycin and ciprofloxacin at 10 \times MIC and corresponding fractions of condensed and lysed cells after treatment for 24 h. Each timepoint represents two biological replicates and, for population fractions, two different fields of view with at least 100 cells each (untreated, 109 and 100 cells; kanamycin, 113 and 102 cells; ciprofloxacin, 175 and 120 cells). For population fractions, a population of cells was treated with antibiotics for the indicated treatment times inside a microfluidic chamber, cells were washed with drug-free medium, and the number of condensed and lysed cells after 20 h were counted. Error bars indicate one standard deviation, and data are presented as mean \pm SEM. **b** *E. coli* cell length (L) traces of 20 cells treated continuously with ciprofloxacin at 10 \times MIC inside a microfluidic chamber. **c** Average normalized single-cell elongation rates ($dL/(Ldt)$) of cells corresponding to panel (**b**), with pre-condensation (pre-) and post-condensation (post-) values shown. Here and below, box plots indicating the median (center), 25th and 75th percentile (bounds of box), and extreme data points not considered outliers (bounds of whiskers) are shown, and red crosses indicate outliers including the minimum and maximum values. p -values for two-sample Kolmogorov-Smirnov tests are shown next to corresponding brackets. **d–e** Same as (**b**, **c**), but for treatment with kanamycin at 10 \times MIC, for which cells exhibited cell length oscillations approximately described by a typical period of $\phi = 20$ min (inset). Box plot features refer to those of panel (**c**). **f**, **g** Same as (**b**, **c**), but for transient antibiotic treatment and subsequent washout, showing that recovering, turgid cells survive and continue to elongate. Here, time is defined as time since condensation for condensed cells and time since start of measurement for recovering cells. Cell length represents cumulative cell length of a cell and, if the cell divides, all its progeny. The length is normalized to its value at condensation for condensed cells and to its starting length for recovering cells. All cells were treated for 30 min with kanamycin or ciprofloxacin at 10 \times MIC inside a microfluidic chamber. Box plot features refer to those of panel (**c**).

antibiotics, including aminoglycosides and fluoroquinolones, is associated with cellular metabolism^{24,25}. As cellular metabolism is decreased in stationary-phase cells (Supplementary Fig. 12), the decreased frequencies of condensation and lysis—in addition to decreased killing—observed in these cells are consistent with the finding that these cells are less susceptible to antibiotics.

Cytoplasmic condensation is associated with ROS accumulation, lipid peroxidation, and changes in lipid composition.

Although membrane damage and cytoplasmic condensation occur rapidly after antibiotic exposure, inhibition of DNA replication and protein translation, by themselves, are not known to lead to membrane damage, prompting our inquiry into the underlying mechanism of these phenotypes. While aminoglycosides have been shown to perturb membranes through non-specific ionic bonds and misfolded proteins^{26–28}, another possibility that may explain our observations with both aminoglycosides and fluoroquinolones is that promiscuously reactive metabolic by-products damage membrane phospholipids through processes involving, for example, free-radical reactions^{2,3,13,29}. Previous work has shown that antibiotic-treated cells experience increased flux through metabolic pathways that lead to reactive metabolic by-products irrespective of the primary antibiotic-binding target, and these reactive metabolic by-products have been evidenced to contribute to antibiotic lethality^{2–13,29}. Indeed, consistent with this notion, we observed that condensed and/or lysed antibiotic-treated cells exhibited significantly elevated levels of reactive oxygen species (ROS) and reactive nitrogen species (RNS), as measured by the dyes carboxy-H₂DCEFDA and DAF-FM (Fig. 4a, b).

As such, we wondered whether cytoplasmic condensation specifically correlated with lipid peroxidation, a process in which free radicals and other reactive molecules react with fatty acids and may ultimately rupture the membrane³⁰. To test this hypothesis, we assayed lipid peroxidation both in single cells and bulk culture using the lipophilic dye C11-BODIPY. The fluorescence of this dye shifts from red to green when oxidized by oxy-radicals and peroxynitrite³¹, and measurements of green fluorescence intensity over time offer a quantitative measure of lipid peroxidation dynamics. Consistent with the hypothesis that cytoplasmic condensation correlates with lipid peroxidation, we observed that condensed and lysed cells exhibited larger intensities than turgid cells (Fig. 4c). Moreover, cells exhibited sharp increases in fluorescence coincident in time with condensation and lysis (Fig. 4d). Flow cytometry measurements using bulk cultures also confirmed an increase in fluorescence, implying increases in ROS and RNS, consistent with single-cell measurements (Fig. 4e–g).

As the foregoing results indicate changes in membrane composition, we next characterized the lipid contents of antibiotic-treated cells (Fig. 5). We found that bulk cultures treated with kanamycin and ciprofloxacin, in addition to bulk cultures treated with ampicillin and 10 mM H₂O₂ considered here for comparison, exhibited detectable increases in free fatty acids (FFA) relative to untreated cells (Fig. 5a). In particular, averaged measurements of peak area intensities suggest that FFA levels are increased by as much as ~1-fold in kanamycin and ciprofloxacin-treated cells and by as much as ~7-fold in ampicillin-treated cells, with the size of the increase varying with treatment time (Fig. 5b). While the latter may be expected based on the lytic mode of action of ampicillin, the observation of increased FFA levels in kanamycin- and ciprofloxacin-treated cells contrasts with the primary modes of action of aminoglycosides and fluoroquinolones and is consistent with the membrane damage characterized above using SYTOX Blue (Fig. 1g). We also observed salient shifts

in cardiolipin (CL)/phosphatidylethanolamine (PE) ratios (Fig. 5a, c), which have previously been shown to be associated with changes in cell envelope ultrastructure similar to that found for cytoplasmic condensation here³². Indeed, we found that CL/PE ratios could be ~2 to ~3-fold higher in kanamycin- and ciprofloxacin-treated cells, suggesting that antibiotic treatment and subsequent cytoplasmic condensation may be generally associated with changes in the CL/PE ratio and lipid composition. In sum, these results are consistent with our observations of membrane damage, and together our experiments demonstrate that antibiotic-induced cytoplasmic condensation is associated with the accumulation of promiscuously reactive metabolic by-products (Fig. 4), lipid peroxidation (Fig. 4), and changes in lipid composition (Fig. 5).

Finally, as previous work has shown that excess lipopolysaccharide (LPS) can lead to cell death in a *mfa** strain of *E. coli*³³, we asked as well whether changes in LPS levels are associated with the cell death phenotype characterized here. Measuring LPS concentrations in antibiotic-treated bulk cultures with a limulus amoebocyte lysate (LAL) assay, we found, intriguingly, that kanamycin- and ciprofloxacin-treated cultures exhibited significantly lower LPS concentrations than did untreated cultures (Supplementary Fig. 13). This observation suggests that increased LPS levels may not be associated with cell death in cells treated with kanamycin and ciprofloxacin.

Cytoplasmic condensation and antibiotic-induced cell death are mitigated by glutathione, a scavenger of reactive metabolic by-products.

We next sought to determine whether the reactive metabolic by-products that are associated with cytoplasmic condensation also contribute to antibiotic lethality, as measured at the single-cell level by the frequency of condensation and lysis as well as in bulk culture by time-kill assays. To this end, we pre-treated growing cultures of *E. coli* with glutathione, an antioxidant and scavenger of reactive metabolic by-products that is also known to attenuate antibiotic killing of bulk cultures^{13,24}. We observed significantly decreased killing by both kanamycin and ciprofloxacin in glutathione-pretreated cultures (Fig. 6a, b). Specifically, exogenous supplementation of glutathione (10 mM) decreased kanamycin killing by as much as ~7 logs and ciprofloxacin killing by as much as ~4 logs for cell cultures treated at the previously determined MICs. As glutathione also increases the MICs of kanamycin and ciprofloxacin (Supplementary Table 1), we performed further time-kill assays relative to these increased MICs (Fig. 6a, b). These assays revealed increased survival relative to cases of no glutathione with kanamycin treatment in the range of 1× MIC and ciprofloxacin treatment at various treatment times in the range of 0.1× to 10× MIC (Fig. 6a, b), suggesting that the glutathione protection observed in bulk cultures may arise from both decreasing growth inhibition and decreasing killing of individual cells. At the single-cell level, antibiotic treatment of glutathione-pretreated cells was accompanied by cell proliferation in kanamycin-treated cells and notable suppression of condensation and lysis in ciprofloxacin-treated cells (Fig. 6c, h and Supplementary Movies 6 and 7), suggesting a reactive metabolic by-product-based origin for the membrane damage and decreased survival observed in the absence of glutathione. Furthermore, while antibiotic lethality correlates with cellular metabolism^{24,25,29}, we note here that the observed protection from antibiotic killing by glutathione did not arise from differences in intracellular ATP levels, as indicated by bulk-culture measurements of ATP abundance (Supplementary Fig. 12). Indeed, since glutathione is involved not only in ROS and RNS scavenging but also cellular detoxification of additional reactive metabolic by-products such as methylglyoxal³⁴, these results

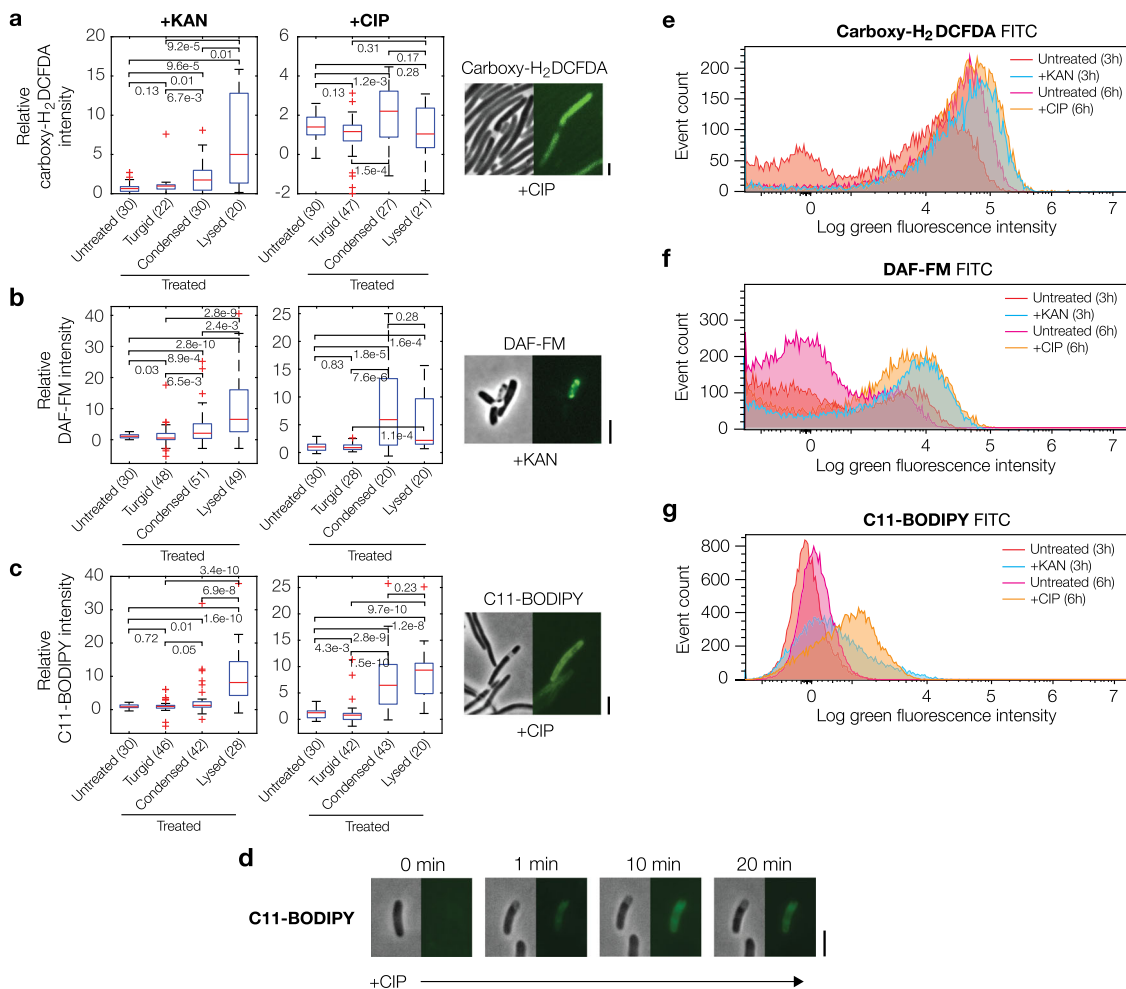


Fig. 4 Cytoplasmic condensation is associated with the accumulation of reactive metabolic by-products. **a** Fluorescence intensities of antibiotic-treated *E. coli* in the presence of the ROS-sensitive dye carboxy-H₂DCFDA. A representative view of ciprofloxacin-treated cells imaged in phase contrast and epifluorescence is shown. Here and below, the kanamycin and ciprofloxacin concentrations used were 10× MIC, error bars represent one standard deviation, and scale bars indicate 3 μm. The number of cells in each group are indicated in parentheses. Box plots indicating the median (center), 25th and 75th percentile (bounds of box), and extreme data points not considered outliers (bounds of whiskers) are shown, and red crosses indicate outliers including the minimum and maximum values. *p*-values for two-sample Kolmogorov-Smirnov tests are shown next to corresponding brackets. **b, c** Same as **(a)**, but for DAF-FM, a dye sensitive to nitric oxide **(b)**, and C11-BODIPY, a lipid peroxidation-sensitive dye **(c)**. **d** A representative timelapse of a ciprofloxacin-treated *E. coli* cell in the presence of C11-BODIPY. Times show duration after the first image, and results are representative of three biological replicates. **e–g** Histograms of fluorescence intensities of populations of control and antibiotic-treated *E. coli*, as assayed by flow cytometry using the FITC fluorochrome. Dyes and antibiotic concentrations were the same as in **(a–c)**, and cells were assayed after 3 h (untreated and kanamycin-treated cells) and 6 h (untreated and ciprofloxacin-treated cells) of treatment. Cells were analyzed after longer times for ciprofloxacin treatment because a majority of condensation events occurred later in time (Fig. 1d). Data are representative of four biological replicates and 20,000 scattering events for each distribution.

suggest that reactive metabolic by-products—which may include, but are not limited to, ROS and RNS—contribute to antibiotic-induced cell death, and that glutathione-mediated detoxification of these molecules contributes to protection from antibiotic lethality.

Next, we performed time-kill experiments on Δ *gor* and Δ *gshA* strains of *E. coli*, which, respectively, lack genes encoding for glutathione reductase (Gor) and a glutamate-cysteine ligase (GshA) contributing to glutathione synthesis^{35,36}. We found that antibiotic lethality remained largely unchanged from wild-type controls, suggesting that the modifications to intracellular glutathione pools arising from these genetic deletions have limited effects on aminoglycoside and fluoroquinolone killing (Supplementary Fig. 14). As endogenous pools of glutathione have been estimated to be ~10 mM in *E. coli*³⁷, it is possible that these genetic perturbations induce smaller variations in glutathione concentration than are needed to protect against

antibiotic lethality resulting from the production of reactive metabolic by-products.

As a positive control for a scavenging reaction involving glutathione, we repeated our time-kill experiments with treatment by exogenous peroxynitrite³⁸ with and without pretreatment by glutathione (10 mM). To explore the effects of different antioxidants, we also considered the antioxidants dithiothreitol and mercaptoethanol (10 mM). Intriguingly, treating exponentially growing bulk cultures with peroxynitrite resulted in several logs of killing, which was accompanied at the single-cell level by cytoplasmic condensation and lysis (Fig. 6d–f). Yet, while pretreatment with any of the three antioxidants considered rescued cells from peroxynitrite killing and appeared to suppress peroxynitrite-induced cytoplasmic condensation and lysis (Fig. 6e, f, h), we found that cells pretreated with dithiothreitol and mercaptoethanol were not substantially rescued from kanamycin and ciprofloxacin-induced cell death and cytoplasmic

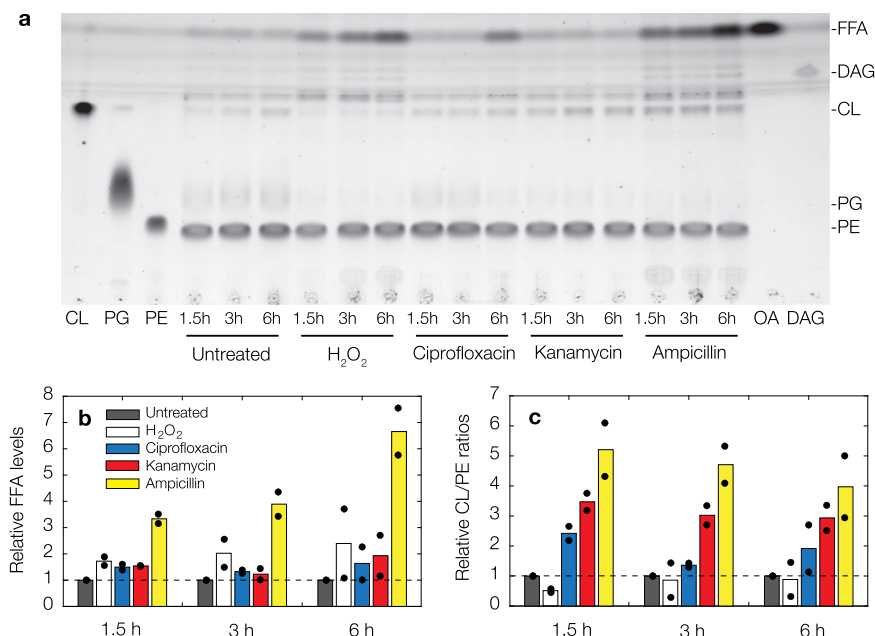


Fig. 5 Antibiotic treatment is associated with changes in lipid composition. **a** Representative thin-layer chromatography image for lysates of control and antibiotic-treated cell cultures. Cells were harvested after various treatment times as shown, and antibiotic concentrations used were 10× MIC. For comparison, results for cells treated with 10 mM hydrogen peroxide and 10× MIC ampicillin are shown. Results are representative of two biological replicates. Abbreviations: CL, cardiolipin; PG, phosphatidylglycerol; PE, phosphatidylethanolamine; FFA, free fatty acids; DAG, diacylglycerol; OA, oleic acid. **b, c** Relative FFA levels (**b**) and CL/PE ratios (**c**) across treatment conditions, relative to values for untreated cells at each treatment time. Data are from two biological replicates (black points), and bars indicate averages.

condensation (Fig. 6g, h). Consistent with these observations, kanamycin and ciprofloxacin MICs were unchanged in the presence of dithiothreitol and mercaptoethanol (Supplementary Table 1). These differences, which could arise from varied scavenging potentials toward different reactive metabolic by-products, suggests that aminoglycoside and fluoroquinolone-induced cytoplasmic condensation, lysis, and cell death may not be explained by the accumulation of peroxyxynitrite alone.

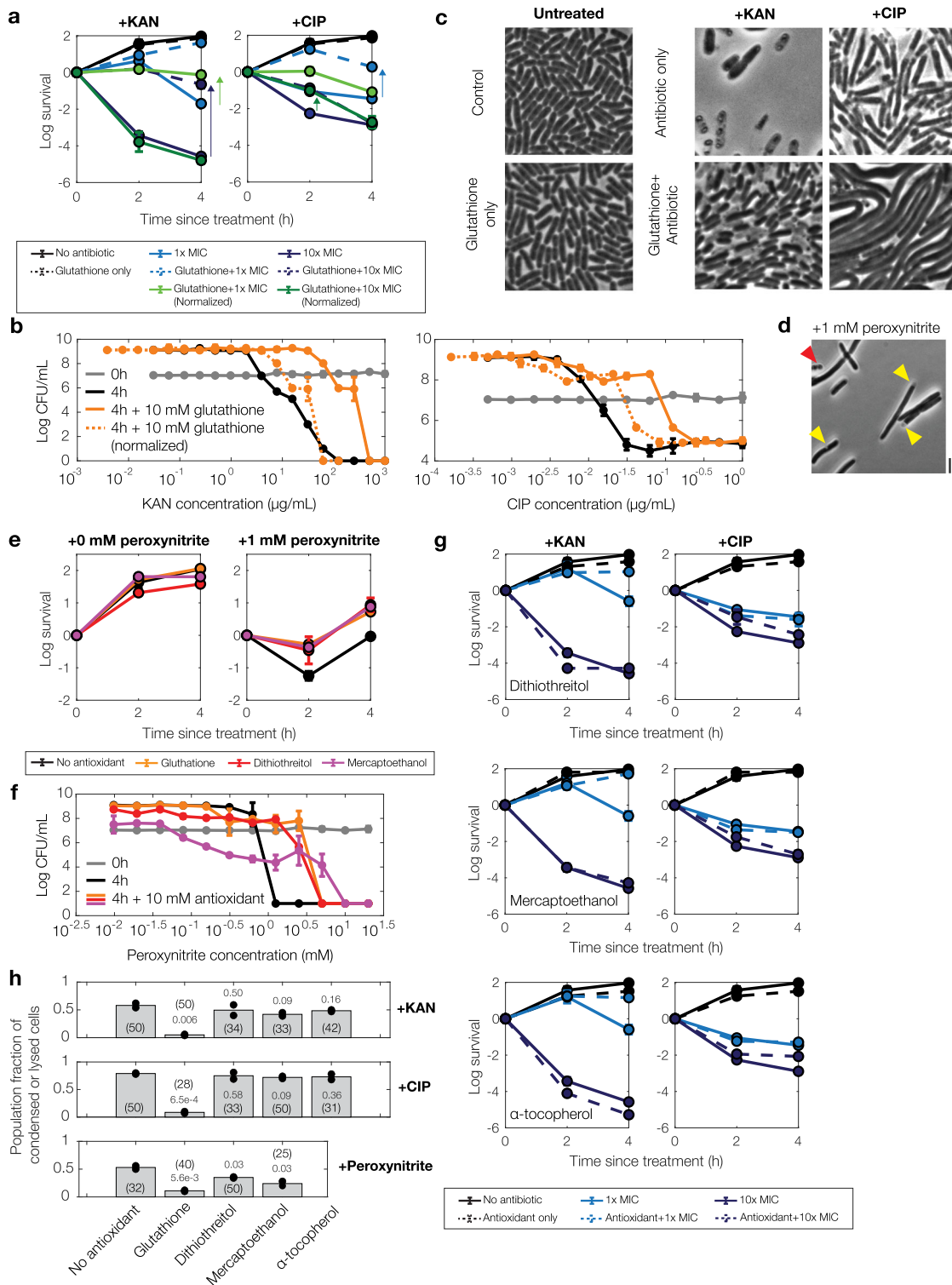
Finally, in order to test whether certain compounds might attenuate lipid peroxidation and cell death in antibiotic-treated cells, we performed microscopy and time-kill experiments involving the exogenous supplementation of α -tocopherol, a lipophilic antioxidant which has been shown to mitigate lipid peroxidation in eukaryotes³⁹. We found that pretreating with α -tocopherol (50 mM) did not significantly alleviate antibiotic lethality (Fig. 6g) or alter kanamycin and ciprofloxacin MICs (Supplementary Table 1). Consistent with our characterization of cytoplasmic condensation as a cell death phenotype, cytoplasmic condensation and fluorescence of C11-BODIPY also occurred similarly to cells without α -tocopherol pretreatment (Fig. 6g, h and Supplementary Fig. 15). We speculate that α -tocopherol may be less potent in *E. coli* than in eukaryotes due to potentially limited scavenging potential and uptake. Intriguingly, a recent study developed a lipophilic antioxidant different from α -tocopherol and showed that it prevented lipid peroxidation and fluoroquinolone-induced cell death in *E. coli*⁴⁰; together with our results, this observation suggests a varied landscape of chemical compounds that could attenuate lipid peroxidation and, in doing so, mitigate antibiotic lethality.

Cytoplasmic condensation and antibiotic-induced cell death are robust to changes in oxygen availability and external osmolarity. As the foregoing results suggest that cytoplasmic condensation and antibiotic-induced cell death are associated with membrane damage induced by reactive metabolic by-products, we asked how cytoplasmic condensation and antibiotic

lethality could be affected by perturbations including (1) the absence of environmental oxygen; and (2) osmotic shifts that might physically restore cellular turgor and reverse the condensed phenotype. To address this question, we performed microscopy and time-kill experiments.

We first considered the effects of oxygen availability on our findings. We performed microscopy and time-kill experiments in an anaerobic chamber similarly to previous work from our group¹³. Intriguingly, when cells were cultured, treated, and imaged under strictly anaerobic conditions, we found that treatment by kanamycin and ciprofloxacin still induced cytoplasmic condensation and fluorescence of C11-BODIPY (Fig. 7a). Surprisingly, however, we found that glutathione also conferred protection in anaerobic time-kill assays (Fig. 7b), suggesting that glutathione may be involved in cellular detoxification in the absence of environmental oxygen. Survival of glutathione-pretreated bulk cultures under kanamycin treatment was increased similarly to aerobic conditions, by ~3 logs at 10× the baseline aerobic MIC, while survival under ciprofloxacin treatment was increased by ~1 to 2 logs at 1× and 10× MIC (Fig. 7b). Together, these findings indicate that reactive metabolic by-products in addition to ROS, including RNS¹³, may contribute to cytoplasmic condensation and antibiotic-induced cell death under anaerobic conditions.

We next performed microfluidic and time-kill experiments in which antibiotic-treated cells were hypoosmotically shocked, in order to produce increases in cellular turgor. In microfluidic experiments, cells were grown in LB with 250 mM sorbitol before and during ~3 h of treatment with kanamycin or ciprofloxacin (at 10× MIC). At the onset of cytoplasmic condensation, cells were hypoosmotically shocked with a flow of sorbitol-free, drug-containing LB. In untreated controls, this hypoosmotic shock results in the transient enlargement of cells due to increased turgor, with typical cytoplasmic volume increases of less than ~5%⁴¹, as confirmed here (Supplementary Movie 8). In most antibiotic-treated cells, we found that this



hypoosmotic shock did not change the condensed phenotype. Nevertheless, we found that a small fraction (~10%) of condensed, ciprofloxacin-treated cells briefly became turgid, as indicated in phase-contrast by phase-light regions becoming phase-dark and increases in cell size, so that hypoosmotic shock appeared to transiently reverse cytoplasmic condensation in these cells (Fig. 7c and Supplementary Movie 9). Yet, after several minutes—a timescale consistent with the timescale of solute outflow predicted by our model—these cells reverted to the condensed phenotype and failed to elongate upon

continued observation. In contrast to ciprofloxacin-treated cells, we observed typical kanamycin-treated cells to lyse immediately after hypoosmotic shock (Supplementary Movie 10), as would be consistent with a scenario in which kanamycin-induced membrane damage is more widespread—potentially due to ribosome-independent ionic interactions with the outer membrane^{20,26}—and results in a lower resistance of the membranes to stretching. Importantly, for both antibiotics, application of hypoosmotic shock failed to rescue cells by resulting in continued cell growth.

Fig. 6 Cytoplasmic condensation and antibiotic killing vary with the supplementation of glutathione, an antioxidant, but not dithiothreitol, mercaptoethanol, or α -tocopherol. **a, b** Survival curves of *E. coli* under kanamycin and ciprofloxacin treatment with and without exogenous supplementation of glutathione (10 mM), as determined by CFU plating and counting. Each point represents two biological replicates, error bars indicate one standard deviation, and data are presented as mean \pm SEM. Positive survival values indicate increases in CFU/mL. Measurements at 1 \times and 10 \times MIC (**a**) and endpoint measurements (**b**) across a range of antibiotic concentrations are shown. Arrows highlight protection. All MICs used were with respect to their baseline values, with the exception of increased concentration values adjusted for growth inhibition effects (“normalized”), as summarized in Supplementary Table 1. **c** Phase-contrast microscopy images of control and antibiotic-treated *E. coli* (10 \times MIC) with and without exogenous supplementation of glutathione (10 mM), taken -10 h after continual antibiotic treatment. The starting densities of cells are similar across all images, and results are representative of two biological replicates. Scale bar, 3 μ m. **d** Same as (**c**), but for treatment with peroxyntirite, a reactive metabolic by-product. Cells were imaged 3 h after treatment with peroxyntirite. Results are representative of two biological replicates. **e, f** Same as (**a, b**), but for peroxyntirite treatment and exogenous supplementation of glutathione (10 mM), dithiothreitol (10 mM), and mercaptoethanol (10 mM). **g** Same as (**a**), but for kanamycin and ciprofloxacin treatment and exogenous supplementation of dithiothreitol (10 mM), mercaptoethanol (10 mM), and α -tocopherol (50 mM). **h** Fractions of all cells that are condensed or lysed 6 h after antibiotic treatment (10 \times MIC) or peroxyntirite treatment (1 mM) and antioxidant pretreatment (glutathione, dithiothreitol, mercaptoethanol: 10 mM; α -tocopherol: 50 mM). Data from two different fields of view from two biological replicates; individual data points from fields of view are shown. The number of cells in each field of view in each group are indicated in parentheses, and *p*-values for two-sample *t*-tests for differences in mean value compared to cases with no antioxidant are shown next to cell numbers.

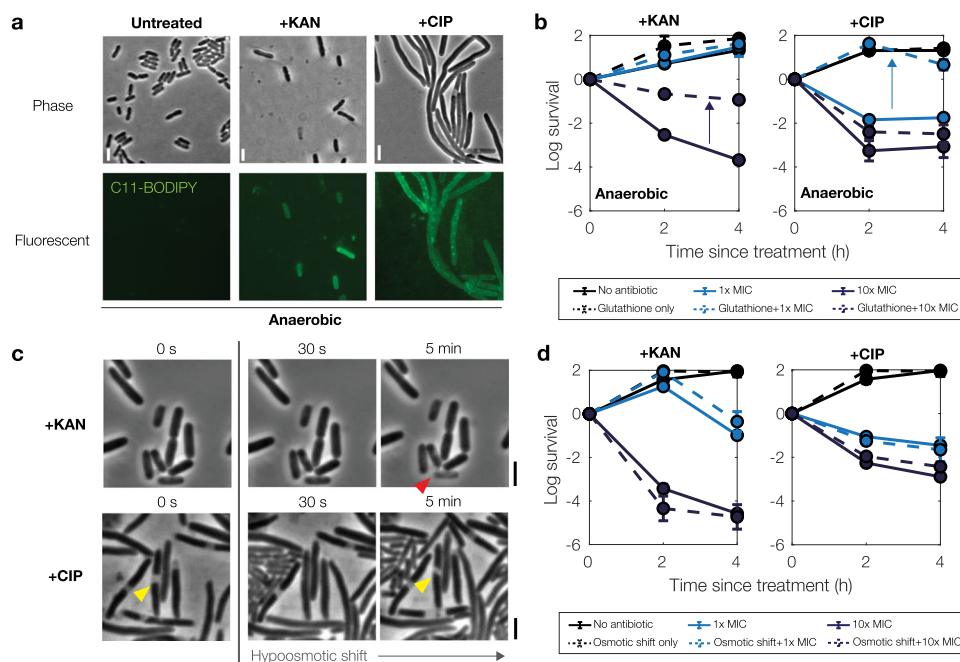


Fig. 7 Cytoplasmic condensation and antibiotic killing are robust to changes in oxygen availability and external osmolarity. **a** Phase-contrast and fluorescence microscopy images of control and antibiotic-treated *E. coli* (10 \times MIC) taken 3 h after treatment. Cells were grown, treated, and imaged under anaerobic conditions in LB medium. Scale bar, 3 μ m. **b** Survival curves of *E. coli* under anaerobic kanamycin and ciprofloxacin treatment, as determined by CFU plating and counting. Each point represents two biological replicates, error bars indicate one standard deviation, and data are presented as mean \pm SEM. Positive values indicate increases in CFU/mL. Arrows highlight protection. All MICs used were with respect to their baseline values under aerobic conditions (Supplementary Table 1). **c, d** Same as (**a, b**), but for aerobic cell cultures that are hypoosmotically shocked by downshifting from 250 mM sorbitol after -3 h of antibiotic treatment (**c**) and at plating (**d**). Yellow and red markers highlight condensed and lysed cells, respectively.

In corresponding time-kill experiments, bulk cultures were treated with kanamycin or ciprofloxacin (10 \times MIC) in LB with 250 mM sorbitol. Cells were then hypoosmotically shocked by serial dilution in LB before plating on drug- and sorbitol-free LB agar. Consistent with our microscopy observations, subsequent CFU quantitation showed that cellular survival was not significantly changed in these cultures relative to the case of no osmotic shift at the time of plating (Fig. 7d). Together, these results suggest that physical changes in turgor pressure do not mitigate kanamycin- and ciprofloxacin-induced cell death and membrane damage. These findings are also consistent with the hypothesis that reactive metabolic by-product-mediated membrane damage lies upstream of cytoplasmic condensation and cell death.

Discussion

In summary, our results, which include both single-cell biophysical and conventional bulk-culture approaches, suggest the following physical biology-based model of bacterial cell death. Upon the primary antibiotic-target interaction, cells generate reactive molecules from increased flux through metabolic pathways including glycolysis and the tricarboxylic acid cycle, as previously reported³. These reactive metabolic by-products lead to cellular damage by promiscuously reacting with nucleic acids, proteins, and membrane lipids. Reactions with the membrane in processes including lipid peroxidation induce loss of membrane integrity, which results in cytoplasmic condensation through the leakage of cytoplasmic contents and coincides with the loss of viability in cells. Intriguingly, because cytoplasmic condensation is not seen

in all dead cells, our results suggest that alternative cell death pathways—which may involve cellular damage to nucleic acids and proteins resulting from both the primary drug–target interaction and subsequent generation of reactive metabolic by-products—also contribute to antibiotic-induced cell death.

The phenotype of cytoplasmic condensation described in this work may offer a way of diagnosing bacterial cell death, in addition to suggesting possible molecular pathways that contribute to antibiotic lethality. Our observation that condensed cells no longer accumulate biomass at the time of condensation suggests, consistent with recent work from the Zhao and Drlica groups¹¹, that antibiotic-treated cells can die substantially after antibiotic treatment, and that this cell death is not revealed by traditional time-kill experiments in which cells are assumed to have died at the time of plating. As our observations indicate that condensed cells are effectively dead, screening for cytoplasmic condensation may inform a phenotype-based approach to antibiotic susceptibility testing, which typically involves cell culturing and genetic sequencing or intensive time-kill assays.

Finally, we observed that treatment by aminoglycoside and fluoroquinolone antibiotics, in contrast to their primary modes of action, is associated with membrane damage, lipid peroxidation, and changes in lipid composition. The observation that cytoplasmic condensation and lipid peroxidation can occur under different oxygen conditions, and are variably influenced by the application of different antioxidants, suggests that a complex landscape of reactive metabolic by-products may contribute to antibiotic lethality. Further work is needed to characterize these reactive metabolic by-products and the different cell death pathways in which they participate. The present study addresses this issue, in part, by showing a sequence of cellular events that can lead to antibiotic-induced cell death, underscoring cytoplasmic condensation as a terminal cell death phenotype in antibiotic-treated cells. Intriguingly, comparable cell death phenotypes have been observed in modes of killing as diverse as carbon starvation⁴² and copper alloy treatment⁴³, suggesting that cytoplasmic condensation may be a common phenotype accompanying bacterial cell death.

Methods

Bacterial strains. The wild-type strain of *E. coli* used in this study, unless otherwise specified, is MG1655; we verified similar results in W3110 and BW25113. Strains with fluorescently tagged cytoplasmic and cell envelope components used in this study comprise those tagged as follows: cytoplasmic mCherry (DH5α(*lpir*), pTD47), ZipA-mCherry (inner membrane-tagged, TB28, attHKNP5)⁴⁴, LpoB-GFP (MG1655, attHKCB28; outer membrane-tagged)⁴⁴ and ssDsbA-LpoB-GFP (TB28, attHKCB41; periplasm-tagged)⁴⁵; these strains were a gift from the Bernhardt group and cultured in the absence of antibiotics. The *DgshA* (JW2663-1) and *Dgor* (JW3467-1) strains were from the Keio collection of non-essential single knockouts⁴⁶. For *B. subtilis*, strain 168 (ATCC 23857) was used.

Antibiotics and other reagents. Kanamycin sulfate (product 60615, MilliporeSigma, St. Louis, MO), gentamicin sulfate (MilliporeSigma G1914), mecillinam (MilliporeSigma 33447), and ampicillin sodium salt (MilliporeSigma A9518) were dissolved in ultrapure Milli-Q water. Ciprofloxacin powder (MilliporeSigma 17850) was dissolved in dilute acid (0.1 M HCl). Norfloxacin (MilliporeSigma N9890) was dissolved in dimethyl sulfoxide (DMSO, MilliporeSigma D5879). All antibiotics were freshly prepared before each experiment.

L-glutathione (reduced, MilliporeSigma G4251) and sorbitol were dissolved in ultrapure Milli-Q water. Solutions of DL-dithiothreitol (MilliporeSigma D0632) and 2-mercaptoethanol (MilliporeSigma M6250) were also prepared with ultrapure Milli-Q water. (+/-)-α-tocopherol (MilliporeSigma T3251) was dissolved in ethanol. Peroxynitrite (MilliporeSigma 516620) was used as supplied. All of these reagents were freshly prepared before each experiment.

Bacterial culture and growth. Cells were grown in liquid LB medium (product 244620, Becton Dickinson, Franklin Lakes, NJ). LB media containing 1.5% Difco agar (Becton Dickinson 244520) was used to grow individual colonies. Cells were grown from single colonies at 37 °C either in tubes in an incubation chamber shaking at 300 rpm or, for determining MICs, in 96-well plates (product 9018, Corning, Corning, NY) sealed with breathable membranes (MilliporeSigma

Z763624) with shaking at 900 rpm. For Supplementary Fig. 12, LB medium was diluted in phosphate-buffered saline (PBS; Corning 21-040).

Determination of MICs. We determined MICs for all antibiotics considered in this work by diluting both 1:100 and 1:10,000 from an overnight culture into both 96-well plates and 14-mL Falcon tubes with varying antibiotic concentrations. The MIC was determined as the minimum concentration at which no visible growth occurred overnight (12–18 h; OD₆₀₀ < 0.1). OD₆₀₀ values were measured in 14 mL Falcon tubes with a Biowave cell density meter CO8000 (Biochrom, Holliston, MA) and in 96-well plates, using 200 μL working volumes, with a SpectraMax M3 plate reader (Molecular Devices, San Jose, CA). A summary of all MIC values thus determined and their working values for different bacterial strains are provided in Supplementary Table 1, and we note here that we found quantitatively similar MIC values between 1:100 and 1:10,000 dilutions, which lie within the tabulated ranges shown in Supplementary Table 1.

Microscopy. Microscopy experiments were performed with cells sandwiched between agarose pads and glass coverslips or slides unless otherwise stated. Cells were concentrated by centrifugation at 850g for 5 min and resuspended in a smaller volume of supernatant. We placed 2 μL of the resuspended bacterial culture between either 3" × 1" × 1" microscope slides (product 125444, Fisher Scientific, Hampton, NH) or number 1.5 coverslips (VWR, Radnor, PA) and 1 mm thick agarose (1.5%) pads made from growth media (agarose: type IX-A, MilliporeSigma A2576), following conventional procedures for immobilizing cells⁴⁷. Cells were imaged immediately afterward. We used a Nikon Ti inverted microscope (Nikon, Tokyo, Japan) equipped with a 6.5 μm-pixel Hamamatsu CMOS camera (Hamamatsu, Hamamatsu City, Japan), a Nikon 100× NA 1.45 objective, TIRF illumination, and an enclosing custom-made incubation chamber and a Zeiss Axiovert 200 inverted microscope equipped with a Zeiss AxioCam 503 camera, a 40× objective (EC Plan-neofluar, NA 0.75), a 63× objective (EC Plan-neofluar, NA 1.25), and an enclosing custom-made incubation chamber for microfluidic experiments and fluorescence microscopy experiments. AFM experiments were performed with a Zeiss AxioObserver D1 (Zeiss, Jena, Germany), as mentioned below. For all other experiments and replicate fluorescence microscopy experiments, we used a Zeiss AxioScope A1 upright microscope equipped with a Zeiss AxioCam 503 camera, a Zeiss 100× NA 1.3 Plan-neofluar objective (Zeiss, Jena, Germany), and an X-Cite 120Q Iris FL light source (Excelitas Technologies, Salem, MA). For timelapse measurements, cells were imaged at 37 °C inside incubation chambers. Images were recorded using Zen Lite Blue (Zeiss), NIS-Elements (Nikon), and AxioVision (v.4.8, Zeiss) software. We used ImageJ (NIH, Bethesda, MD) for processing and analyzing timelapses and the StackReg plugin⁴⁸, which recursively aligns images in a sequence with geometric transformations, to correct for microscope drift as necessary. Epifluorescence exposure times were limited to a maximum of 300 ms to avoid photobleaching. All microscopy experiments were replicated at least twice, and we verified that the absolute values of all fluorescence intensities were comparable across experiments performed using the same microscopy setup.

Microfluidics and osmotic shock experiments. We used the CellASIC ONIX platform (MilliporeSigma, Burlington, MA) and the associated bacterial microfluidic plate (B04A-03). Cells were grown in culture to early log phase, optical density (OD₆₀₀) between 0.1 and 0.2, or stationary phase, OD₆₀₀ approximately 2, as described below, as measured in 14 mL Falcon tubes with a Biowave cell density meter CO8000. Cells were then loaded into the microfluidic chamber according to the manufacturer's instructions at a flow rate corresponding to 20 kPa (~10 μL/h). For antibiotic treatment, LB containing antibiotics was flowed in from two inlets at a flow rate corresponding to 20 kPa (~10 μL/h); under these settings, we verified that the solution saturated the device in approximately 5 min by adding yellow-green fluorescent beads (0.02 μm diameter; FluoSpheres F8760, Thermo-Fisher, Waltham, MA) to the solution as a proxy for its concentration. Cells were subjected to the same flow continuously unless otherwise noted. For wash-out experiments, fresh LB without antibiotics was flowed in from two inlets at a flow rate corresponding to 20 kPa (~10 μL/h) after cells were treated for specified durations by flow of antibiotic-containing LB. For the osmotic shock experiments shown in Fig. 1e, the protocol outlined above was followed with the following modifications. First, cells were cultured in the presence of antibiotic, when applicable, before being loaded into the microfluidic device. Second, after cell loading and equilibration, the flow was replaced by LB + antibiotic + sorbitol (500 mM; D-sorbitol, MilliporeSigma S1876) flowed in from two inlets at a flow rate corresponding to 20 kPa (~10 μL/h). For the osmotic shock experiments shown in Fig. 7c, d, *E. coli* W3110 was cultured in LB + sorbitol (250 mM). Cells were then loaded into the microfluidic device, and treated with constant flow of LB + sorbitol (250 mM) + antibiotic (when applicable) for 2–5 h until the onset of condensation. For washout experiments, the flow was then replaced by LB + antibiotic (when applicable) flowed in from two inlets at a flow rate corresponding to 10–20 kPa (~5 to 10 μL/h).

Atomic force microscopy measurements. A colony of *E. coli* MG1655 or W3110 was grown in LB media overnight at 30 °C with shaking at 220 rpm. A new culture

was then started from the overnight culture with a 1:1000 dilution in fresh LB media and grown at 37 °C with shaking at 220 rpm. At an OD₆₀₀ between 0.1 and 0.2, ciprofloxacin or kanamycin was added to the shaking culture to a final concentration of 10× MIC. After 3–4 h, 100 µL of bacterial solution was aliquoted on a glass-bottom petri dish (FluoroDish, WPI, Sarasota, FL) coated for 1 h in a 10 mM tris buffer solution (pH 8.5) containing 4 mg/mL dopamine hydrochloride (99%, MilliporeSigma H8502) and incubated at room temperature for 30 min. The bacterial cell solution was then carefully removed, and the petri dish was rinsed twice with PBS to remove unbound cells. PBS was then added to the petri dish for AFM measurements in liquid. AFM measurements were conducted using a Nanowizard IV (JPK BioAFM – Bruker Nano GmbH, Berlin, Germany) mounted on an inverted light microscope (AxioObserver D1, Zeiss). Commercial AFM tips with a nominal spring constant of 0.1 N/m (qp-BioAC, CB2, Nanosensors) were used. Images of immobilized bacteria were acquired using the Quantitative Imaging (QITM) mode of the instrument, a force-distance curve-based imaging mode which allowed us to simultaneously acquire several sample parameters (including topography and mechanical properties). The imaging parameter used were: 2 nN set-point, 7 ms pixel time, 400 nm z-length. The manufacturer's (JPK BioAFM – Bruker Nano GmbH) data processing software was used to determine the elastic modulus from approach force-distance curves using the Hertz model modified for a paraboloid indenter⁴⁹:

$$F = \frac{E}{1 - \nu^2} \frac{4\sqrt{R_C}}{3} \delta^{3/2}.$$

Here, F is the applied force, E is the elastic modulus, ν is the Poisson's ratio, R_C is the radius of the tip, and δ is the indentation (vertical tip position). The cantilever was calibrated using routines within the AFM software based on the Sader method⁵⁰. Representative force-distance curves, elastic modulus heatmaps, and cell dimension measurements are provided in Supplementary Fig. 7.

Inference of the cellular turgor pressure from atomic force microscopy measurements.

Following seminal work by Arnoldi et al.⁵¹, it is possible to estimate the turgor pressure of untreated, turgid cells from our AFM measurements. As shown in Supplementary Fig. 7, typical force-indentation curves on such cells indicate the effective spring constant of the AFM tip and the cell envelope as $k_{\text{eff}} \sim 0.03$ N/m. For an AFM tip with spring constant 0.1 N/m and assuming that the effective spring constant arises from two linear springs in series⁵¹, the cell envelope spring constant is ~ 0.04 N/m. The following equation, based on modeling the indentation of a pressurized shell, then relates the cell envelope spring constant to the cellular turgor pressure:

$$k_s = \frac{3\pi}{2} p R \varphi(\rho/d). \quad (1)$$

Here, k_s is the cell envelope spring constant, p is the cellular turgor pressure, R is the cell radius, and $\varphi(\rho/d)$ is a geometric factor, $\varphi(\rho/d) = \rho K_1(\rho/d)/[dK_0(\rho/d)]$, where K_0 and K_1 are modified Bessel functions, ρ is the radius of the contour of the contact of the cantilever tip with the bacterial envelope, and d is a characteristic annealing length of the cell envelope deformation⁵¹. For typical values of $R = 0.4$ µm and $\varphi(\rho/d) \approx 0.2$ relevant to our experiments, Eq. (1) indicates $p \sim 100$ kPa, an estimate quantitatively consistent with previous osmolarity-based studies of turgor pressure in *E. coli*¹⁹ and approximately 3-fold larger than turgor pressure estimates derived from AFM experiments performed on bulging cells, for which cellular protrusions without the peptidoglycan cell wall were indented⁵².

Membrane permeability and depolarization assays. SYTOX Blue Nucleic Acid Stain (product S11348, Invitrogen, Carlsbad, CA), a DNA intercalating dye, was added to incubating liquid cultures and agarose melt to a final concentration of 5 µM to stain cells with and without compromised membranes. DiBAC₄(3) (Invitrogen B438), a fluorescent reporter of membrane potential, was dissolved in DMSO and added to incubating liquid cultures and agarose melt to a final concentration of 10 µg/mL to stain cells with and without depolarized membranes. ION Potassium Green-2 AM (IPG; product ab142806, Abcam, Cambridge, UK), a membrane-permeable dye sensitive to potassium ions, was added to incubating liquid cultures and agarose melt to a final concentration of 40 µM to stain potassium ions in cells.

ROS and RNS detection with fluorescent dyes. For general detection of oxidative stress and ROS (H₂O₂, ROO[•], and ONOO⁻), we used the cell-permeant dye carboxy-H₂DCFDA (Invitrogen C400), which was dissolved in DMSO and added to incubating liquid cultures and agarose melt to a final concentration of 10 µM. For general detection of RNS, and in particular nitric oxide (NO), we used DAF-FM diacetate (Invitrogen D23844), dissolved in DMSO, at a final concentration of 10 µM.

Membrane peroxidation detection with a fluorescent dye. C11-BODIPY 581/591 (Invitrogen D3861), a fluorescent dye-based lipid peroxidation sensor whose fluorescence emission peak shifts from red to green upon lipid peroxidation³¹, was dissolved in DMSO and added to incubating liquid cultures or agarose melt to a final concentration of 10 µM to stain membranes undergoing lipid peroxidation.

Image analysis. Cells were either counted manually or annotated semi-automatically using the MicrobeJ plugin⁵³ in ImageJ (below) to determine features, such as condensation and lysis, and cellular dimensions. Fluorescence was quantitatively analyzed with ImageJ (National Institutes of Health, Bethesda, MD). Briefly, closed cell contours were delineated based on phase-contrast images using MicrobeJ, and ImageJ was used to measure the mean fluorescence pixel intensity within a given contour. The average background fluorescence intensity was subtracted from all measured values, and the relative intensity was calculated by dividing the difference with the average background fluorescence value. Overlay images were generated with Adobe Photoshop (Adobe, San Jose, CA). We were not blinded to allocation in the analysis.

Condensed cells were delineated based on phase-contrast images or a combination of phase-contrast and fluorescence microscopy images, according to the features described in the main text and shown in Fig. 1a, b. The cell volumes shown in Fig. 2f were calculated, excluding cellular poles, by fitting 2D images of cells to bent rods with constant radii along midlines. Variations in cell length and radii across time were recorded using both phase-contrast timelapses and fluorescence timelapses from the cytoplasmic mCherry strain; see Supplementary Fig. 9 for representative traces. We further note that the reported frequencies of cytoplasmic condensation and lysis in Fig. 1d were determined by counting at pre-defined time intervals up to the end of imaging. It is possible that more cells are condensed or lysed than reported—this could occur if cells either became condensed or lysed after imaging or, in the case of condensation, if cells condensed and lysed faster than the time resolution (~ 1 min/frame) of our imaging.

Single-cell traces. Cell lengths were automatically measured in 20 min intervals for Fig. 3b, f and 10 min intervals for Fig. 3d (2 min intervals for the inset) using the MicrobeJ plugin in ImageJ. These measurements were repeated manually as a consistency check; we found that the results were in good quantitative agreement. Cell lengths were determined as the arclengths of cellular midlines, a construction which takes into account cell bending and movement across different frames of a timelapse²². A three-point moving average (four for the inset) was taken to smooth the curves in Fig. 3d using MATLAB (Mathworks, Natick, MA). Normalized growth rates were calculated by taking discrete finite differences of cell lengths.

Sample preparation for thin-layer chromatography experiments. A single colony of *E. coli* W3110 was grown overnight at 30 °C with shaking at 220 rpm. The next morning, a 1:200 dilution of the overnight culture in 100 mL of fresh LB was grown in Erlenmeyer flasks to an OD₆₀₀ of 0.22 at 37 °C with shaking at 220 rpm. At this OD₆₀₀, freshly prepared solutions of ampicillin (final concentration 100 µg/mL; 10× MIC), ciprofloxacin (final concentration 1 µg/mL; 10× MIC), kanamycin (final concentration 50 µg/mL; 10× MIC), and hydrogen peroxide (final concentration 10 mM; 4× the working MIC of 2.5 mM) were added to the cultures. A control (LB only) culture was examined in parallel. The cultures were incubated for 1, 3, and 6 h. At each timepoint, 20 mL samples from each culture were aliquoted, centrifuged at 3770g and 4 °C, and pelleted in a 50 mL Falcon tube. The supernatant was discarded and the pellet was resuspended in 1 mL of fresh LB, then added to a cryovial. The resuspended pellets were centrifuged again at 3770g and 4 °C, the supernatant was again discarded, and the pellet was flash-frozen in liquid nitrogen. The flash-frozen samples were then stored at -80 °C until further processing.

Thin-layer chromatography of lipid content. Frozen cell pellets were resuspended in 300 µL of ultrapure MilliQ-water and lipids were extracted in two steps with (i) 600 µL of chloroform-methanol (10:1, v/v), and (ii) 600 µL of chloroform-methanol (2:1, v/v). The lipid-containing organic phases were pooled and concentrated. Samples were volume-corrected so that each sample had identical amounts of phospholipid content which approximated the membrane lipid fraction. Samples were applied to 10 × 20 cm silica gel 60 HPTLC plates (Merck, Darmstadt, Germany) and chromatographically migrated using (i) chloroform-methanol-glacial acetic acid (65:25:10, v/v/v) over 50% of the running distance (3.5 cm), and (ii) *n*-hexane-diethylether-glacial acetic acid (70:30:1, v/v/v) over 100% of the running distance (7 cm). The lipids were stained with solutions of copper (II) sulfate-orthophosphoric acid or primuline. Peak area intensity measurements were performed on TLC images using ImageJ. The assay was repeated twice.

Time-kill assays and CFU measurements. For all time-kill assays in bulk culture, cells were diluted 1:100 from an overnight culture into 14 mL Falcon tubes containing 2 mL of growth media and incubated either to early log phase (OD₆₀₀ \approx 0.1), to early stationary phase (OD₆₀₀ = 1.0–1.5), or to late stationary phase (OD₆₀₀ > 2.0) in the conditions described above (with shaking at 300 rpm at 37 °C). OD₆₀₀ measurements were taken in 14 mL Falcon tubes with a Biowave cell density meter CO8000 and in 96-well plates, using 300 µL working volumes, with a SpectraMax M3 plate reader. For antioxidant pretreatment, antioxidants were added to growth media 10 min before the addition of antibiotics, when relevant. Antibiotics were added to the final concentrations indicated, and cultures were re-incubated with shaking at 300 rpm at 37 °C. At the indicated times, cells were removed from incubation, aliquoted, and serially diluted in LB and spotted or spread on LB agar. We performed serial dilutions in LB instead of other media, like PBS, in order to

better control for osmolarity and nutrient shifts. For antibiotic concentrations at 10× MIC, cells were also centrifuged at 2350g for 1 min, 90% of the supernatant was removed, and cells were resuspended in a smaller volume before being serially diluted so as to aid in the removal of antibiotics. Petri dishes were allowed to dry at room temperature before incubation at 37 °C overnight (16–24 h). CFUs were then determined by manual counting, and all measurements are based on counts containing at least 10 colonies. Survival was determined by normalizing all CFU/mL measurements to that immediately before antibiotic treatment at time 0 h.

Flow cytometry. Cells were grown and treated with antibiotics as described above. At the indicated times, cells grown in the presence of fluorescent dyes were removed from incubation, aliquoted into 96-well plates, and processed with a CytoFLEX S flow cytometer (Beckman Coulter, Brea, CA). Cells were flowed at a low flow rate (10 µL/min), and 20,000 events were recorded for each sample. Cells were filtered by calibration of forward- and side-scattering measurements based on those of the cytoplasmic mCherry strain, which differs from MG1655 in that its red fluorescence can be used as a ground truth for separating cells from debris (Supplementary Fig. 16). All samples were analyzed at least in biological duplicate. FlowJo software (v10, Becton Dickinson) was used for data post-processing, and fluorescence intensities correspond to those derived from pulse areas.

ATP abundance assay. Intracellular ATP (Supplementary Fig. 12) was quantified using the BacTiter-Glo Microbial Cell Viability Assay (product G8230, Promega, Madison, WI), according to the manufacturer's instructions. Luminescence and absorbance of samples were measured, using 200 µL working volumes, with a SpectraMax M3 plate reader.

Anaerobic chamber. The experiments shown in Fig. 7a, b were performed in an anaerobic chamber (Type B Vinyl, Coy Labs, Grass Lake, MI) equipped with twin palladium catalysts and a Coy Oxygen/Hydrogen Analyzer (Coy Labs) and maintained at 37 °C. A 5% hydrogen in nitrogen gas mix (product NI HY5300, AirGas, Radnor, PA) was used to maintain the steady-state anaerobic environment at less than 5 ppm oxygen. Additionally, a BD BBL GasPak anaerobic indicator (Becton Dickinson), and growth media containing 1 mg/L resorufin (resazurin: MilliporeSigma R7017) as an anaerobic indicator³⁴, were used to ensure strictly anaerobic conditions. All starting cultures were taken from cultures grown overnight inside the anaerobic chamber, and MICs were based on their aerobic values.

For time-kill assays, cells were serially diluted, plated, and grown overnight inside the anaerobic chamber. Cell cultures were treated in early log phase, OD₆₀₀ ≈ 0.02. OD₆₀₀ measurements were taken in 96-well plates, using 300 µL working volumes, with a SpectraMax M3 plate reader. For microscopy experiments, cells were plated and imaged with a Zeiss AxioScope A1 upright microscope, as detailed above; this microscope was used because it could fit inside the anaerobic chamber. Plating and microscopy were performed strictly inside the anaerobic chamber. To ensure strictly anaerobic conditions, cells were not immobilized with LB agarose pads when imaging in the anaerobic chamber, as compared to imaging under aerobic conditions.

To allow for deoxygenation, all materials used in our experiments were brought into the anaerobic chamber at least 24 h before the start of each experiment, with the exception of antibiotics, C11-BODIPY dye, and glutathione. To ensure freshness of these reagents, these reagents were prepared immediately before each experiment, brought into the anaerobic chamber, and equilibrated in open-cap 1.5 mL or 5 mL centrifuge tubes for 1 to 2 h before usage. After the addition of these reagents to growing cultures, we observed that resorufin in the growth media remained strictly colorless, indicating that these reagents did not introduce significant sources of environmental oxygen to our experiments.

Protein concentration and LPS level assays. The LPS levels shown in Supplementary Fig. 13 were assayed as follows. Here, 50 mL of log-phase bulk cultures of *E. coli* MG1655 grown in LB were treated with kanamycin, ciprofloxacin, and ampicillin at 10× MIC for 3 h in 250-mL flasks. Cells were then centrifuged at 3720g for 10 min. Next, the supernatant in all samples was discarded. Each cell pellet was washed with 500 µL PBS, resuspended, and centrifuged again as above; then, the supernatant was discarded from each sample. Next, 500 µL B-PER II (product 78260, Thermo Fisher Scientific, Waltham, MA) containing 100 µg/mL lysozyme (MilliporeSigma L6876) and 5 U/mL DNase I (Thermo Fisher 90083) was added to cell pellets for harvesting, and all samples were vortexed and incubated at 37 °C for an additional 15 min. All samples were then centrifuged at 1500g for 10 min, and the supernatant was aliquoted from each sample for analysis. Serial 1:10, 1:100, 1:10,000, and 1:100,000 dilutions of each cell lysate sample in PBS and endotoxin-free water were generated and used for each of the assays below to ensure that protein and LPS levels were in the range of the standard curves.

To measure the total protein concentration of cell lysates, we used a Pierce BCA protein assay kit (Thermo Fisher 23227) following the manufacturer's instructions. Briefly, the assay reagent was prepared by mixing the assay kit components according to the manufacturer's instructions, and, for each sample, 25 µL of the cell lysate was pipetted directly into a larger volume (200 µL) of reagent in a 96-well plate. All samples were then incubated for 30 min at 37 °C according to the manufacturer's instructions, and the optical density at 562 nm was measured with a

SpectraMax M3 plate reader. Standard curves were generated from control samples with bovine serum albumin (BSA) concentrations of 2000, 1500, 1000, 750, 500, 250, 125, 25, and 0 µg/mL, according to the manufacturer's instructions. To determine the component of protein concentration originating from bacterial cells, the protein concentration of the B-PER II medium with 100 µg/mL lysozyme and 5 U/mL DNase I (measured to be ~140 µg/mL) was subtracted from the calculated protein concentrations in each lysate sample.

To measure the LPS levels of cell lysates, we used a Pierce Chromogenic Endotoxin Quant Kit (Thermo Fisher A39553) following the manufacturer's instructions. Briefly, the assay reagent, based on the LAL, was reconstituted and applied to 50 µL of samples and LPS standards in a 96-well plate. After mixing and incubation, chromogenic substrate was added. Following a final incubation step and addition of 25% acetic acid to each well, the optical density at 405 nm was measured with a SpectraMax M3 plate reader. Standard curves were generated from control samples with LPS concentrations of 1.0, 0.5, 0.25, 0.1, and 0 endotoxin units per mL, according to the manufacturer's instructions.

Statistical testing. Two-sample Kolmogorov-Smirnov tests and one-sample and two-sample *t*-tests were performed at the standard 5% significance level, and *p*-values are indicated when applicable.

Reporting summary. Further information on research design is available in the Nature Research Reporting Summary linked to this article.

Data availability

Additional data that support the findings of this study are available from the corresponding authors upon reasonable request. Source data are provided with this paper.

Received: 8 September 2020; Accepted: 15 March 2021;

Published online: 19 April 2021

References

- Kohanski, M. A., Dwyer, D. J. & Collins, J. J. How antibiotics kill bacteria: from targets to networks. *Nat. Rev. Microbiol.* **8**, 423–435 (2010).
- Belenky, P. et al. Bactericidal antibiotics induce toxic metabolic perturbations that lead to cellular damage. *Cell Rep.* **13**, 968–980 (2015).
- Kohanski, M. A., Dwyer, D. J., Hayete, B., Lawrence, C. A. & Collins, J. J. A common mechanism of cellular death induced by bactericidal antibiotics. *Cell* **130**, 797–810 (2007).
- Dwyer, D. J., Kohanski, M. A., Hayete, B. & Collins, J. J. Gyrase inhibitors induce an oxidative damage cellular death pathway in *Escherichia coli*. *Mol. Syst. Biol.* **3**, 91 (2007).
- Foti, J. J., Devadoss, B., Winkler, J. A., Collins, J. J. & Walker, G. C. Oxidation of the guanine nucleotide pool underlies cell death by bactericidal antibiotics. *Science* **336**, 315–319 (2012).
- Dwyer, D. J., Camacho, D. M., Kohanski, M. A., Callura, J. M. & Collins, J. J. Antibiotic-induced bacterial cell death exhibits physiological and biochemical hallmarks of apoptosis. *Mol. Cell* **46**, 561–572 (2012).
- Davies, B. W. et al. Hydroxyurea induces hydroxyl radical-mediated cell death in *Escherichia coli*. *Mol. Cell* **36**, 845–860 (2009).
- Brynildsen, M. P., Winkler, J. A., Spina, C. S., MacDonald, I. C. & Collins, J. J. Potentiating antibacterial activity by predictably enhancing endogenous microbial ROS production. *Nat. Biotechnol.* **31**, 160–165 (2013).
- Grant, S. S., Kaufmann, B. B., Chand, N. S., Haseley, N. & Hung, D. T. Eradication of bacterial persisters with antibiotic-generated hydroxyl radicals. *Proc. Natl Acad. Sci. USA* **109**, 12147–12152 (2012).
- Morones-Ramirez, J. R., Winkler, J. A., Spina, C. S. & Collins, J. J. Silver enhances antibiotic activity against Gram-negative bacteria. *Sci. Transl. Med.* **5**, 190ra81 (2013).
- Hong, Y., Zeng, J., Wang, X., Drlica, K. & Zhao, X. Post-stress bacterial cell death mediated by reactive oxygen species. *Proc. Natl Acad. Sci. USA* **116**, 10064–10071 (2019).
- Gusarov, I., Shatalin, K., Starodubtseva, M. & Nudler, E. Endogenous nitric oxide protects bacteria against a wide spectrum of antibiotics. *Science* **325**, 1380–1384 (2009).
- Dwyer, D. J. et al. Antibiotics induce redox-related physiological alterations as part of their lethality. *Proc. Natl Acad. Sci. USA* **111**, E2100–E2109 (2014).
- Balaban, N. Q., Merrin, J., Chait, R., Kowalik, L. & Leibler, S. Bacterial persistence as a phenotypic switch. *Science* **305**, 1622–1625 (2004).
- Pribis, J. P. et al. Gamblers: an antibiotic-induced evolvable cell subpopulation differentiated by reactive-oxygen-induced general stress response. *Mol. Cell* **74**, 785–800 (2019).

16. Bos, J. et al. Emergence of antibiotic resistance from multinucleated bacterial filaments. *Proc. Natl Acad. Sci. USA* **112**, 178–183 (2015).
17. Wong, F. & Amir, A. Mechanics and dynamics of bacterial cell lysis. *Biophys. J.* **116**, 2378–2389 (2019).
18. Pilizota, T. & Shaevitz, J. W. Fast, multiphase volume adaptation to hyperosmotic shock by *Escherichia coli*. *PLoS ONE* **7**, e35205 (2012).
19. Cayley, D. S., Guttman, H. J. & Record, M. T. Biophysical characterization of changes in amounts and activity of *Escherichia coli* cell and compartment water and turgor pressure in response to osmotic stress. *Biophys. J.* **78**, 1748–1764 (2000).
20. Martin, N. L. & Beveridge, T. J. Gentamicin interaction with *Pseudomonas aeruginosa* cell envelope. *Antimicrob. Agents Chemother.* **29**, 1079–1087 (1986).
21. Wong, F., Garner, E. C. & Amir, A. Mechanics and dynamics of translocating MreB filaments on curved membranes. *eLife* **8**, e40472 (2019).
22. Wong, F. et al. Mechanical strain sensing implicated in cell shape recovery in *Escherichia coli*. *Nat. Microbiol.* **2**, 17115 (2017).
23. Turner, R. D., Mesnage, S., Hobbs, J. K. & Foster, S. J. Molecular imaging of glycan chains couples cell-wall polysaccharide architecture to bacterial cell morphology. *Nat. Commun.* **9**, 1263 (2018).
24. Lopatkin, A. J. et al. Bacterial metabolic state more accurately predicts antibiotic lethality than growth rate. *Nat. Microbiol.* **4**, 2109–2117 (2019).
25. Lobritz, M. A. et al. Antibiotic efficacy is linked to bacterial cellular respiration. *Proc. Natl Acad. Sci. USA* **112**, 8173–8180 (2015).
26. Kadurugamuwa, J. L., Clarke, A. J. & Beveridge, T. J. Surface action of gentamicin on *Pseudomonas aeruginosa*. *J. Bacteriol.* **175**, 5798–5805 (1993).
27. Davis, B. D., Chen, L. L. & Tai, P. C. Misread protein creates membrane channels: an essential step in the bactericidal action of aminoglycosides. *Proc. Natl Acad. Sci. USA* **83**, 6164–6168 (1986).
28. Kohanski, M. A., Dwyer, D. J., Wierzbowski, J., Cottarel, G. & Collins, J. J. Mistranslation of membrane proteins and two-component system activation trigger antibiotic-mediated cell death. *Cell* **135**, 679–690 (2008).
29. Stokes, J. M., Lopatkin, A. J., Lobritz, M. A. & Collins, J. J. Bacterial metabolism and antibiotic efficacy. *Cell Metab.* **30**, 30312–2 (2019).
30. Cabiscol, E., Tamarit, J. & Ros, J. Oxidative stress in bacteria and protein damage by reactive oxygen species. *Int. Microbiol.* **3**, 3–8 (2000).
31. Drummen, G. P., van Liebergen, L. C., Op den Kamp, J. A. & Post, J. A. C11-BODIPY(581/591), an oxidation-sensitive fluorescent lipid peroxidation probe: (micro)spectroscopic characterization and validation of methodology. *Free Radic. Biol. Med.* **33**, 473–490 (2002).
32. Rowlett, V. W. et al. Impact of membrane phospholipid alterations in *Escherichia coli* on cellular function and bacterial stress adaptation. *J. Bacteriol.* **199**, e00849–16 (2017).
33. Sutterlin, H. A. et al. Disruption of lipid homeostasis in the Gram-negative cell envelope activates a novel cell death pathway. *Proc. Natl Acad. Sci. USA* **113**, E1565–E1574 (2016).
34. Ferguson, G. P., Töttemeyer, S., MacLean, M. J. & Booth, I. R. Methylglyoxal production in bacteria: suicide or survival? *Arch. Microbiol.* **170**, 209–218 (1998).
35. Bessette, P. H., Åslund, F., Beckwith, J. & Georgiou, G. Efficient folding of proteins with multiple disulfide bonds in the *Escherichia coli* cytoplasm. *Proc. Natl Acad. Sci. USA* **96**, 13703–13708 (1999).
36. Fahey, R. C. Glutathione analogs in prokaryotes. *Biochim. Biophys. Acta* **1830**, 3182–3198 (2013).
37. Fahey, R. C., Brown, W. C., Adams, W. B. & Worsham, M. B. Occurrence of glutathione in bacteria. *J. Bacteriol.* **133**, 1126–1129 (1978).
38. Brunelli, L., Crow, J. P. & Beckman, J. S. The comparative toxicity of nitric oxide and peroxynitrite to *Escherichia coli*. *Arch. Biochem. Biophys.* **316**, 327–334 (1995).
39. Traber, M. G. & Atkinson, J. Vitamin E, antioxidant and nothing more. *Free Radic. Biol. Med.* **43**, 4–15 (2007).
40. Martínez, S. R., Duratini, A. M., Becerra, M. C. & Cosa, G. Real-time single-cell imaging reveals accelerating lipid peroxyl radical formation in *Escherichia coli* triggered by a fluoroquinolone antibiotic. *ACS Inf. Dis.* **6**, 2468–2477 (2020).
41. Buda, R. et al. Dynamics of *Escherichia coli*'s passive response to a sudden decrease in external osmolarity. *Proc. Natl Acad. Sci. USA* **113**, E5838–E5846 (2016).
42. Basta, D. W., Angeles-Albores, D., Spero, M. A., Ciemniecki, J. A. & Newman, D. K. Heat-shock proteases promote survival of *Pseudomonas aeruginosa* during growth arrest. *Proc. Natl Acad. Sci. USA* **117**, 4358–4367 (2020).
43. Hong, R., Kang, T. Y., Michels, C. A. & Gadura, N. Membrane lipid peroxidation in copper alloy mediated contact killing of *Escherichia coli*. *Appl. Environ. Microbiol.* **78**, 1776–1784 (2012).
44. Yao, Z., Kahne, D. & Kishony, R. Distinct single-cell morphological dynamics under beta-lactam antibiotics. *Mol. Cell* **48**, 705–712 (2012).
45. Paradis-Bleau, C. et al. Lipoprotein cofactors located in the outer membrane activate bacterial cell wall polymerases. *Cell* **143**, 1110–1120 (2010).
46. Baba, T. et al. Construction of *Escherichia coli* K-12 in-frame, single-gene knockout mutants: the Keio collection. *Mol. Syst. Biol.* **2006**, 0008 (2006).
47. Hussain, S. et al. MreB filaments align along greatest principal membrane curvature to orient cell wall synthesis. *eLife* **7**, e32471 (2018).
48. Thévenaz, P., Ruttimann, U. & Unser, M. A pyramid approach to subpixel registration based on intensity. *IEEE Trans. Image Process.* **7**, 27–41 (1998).
49. Hertz, H. Über die Berührung fester elastischer Körper. *J. Reine Angew. Math.* **92**, 156–171 (1881).
50. Sader, J. E., Larson, I., Mulvaney, P. & White, L. R. Method for the calibration of atomic force microscope cantilevers. *Rev. Sci. Instrum.* **66**, 3789–3798 (1995).
51. Arnoldi, M. et al. Bacterial turgor pressure can be measured by atomic force microscopy. *Phys. Rev. E* **62**, 1034–1044 (2000).
52. Deng, Y., Sun, M. & Shaevitz, J. W. Direct measurement of cell wall stress stiffening and turgor pressure in live bacterial cells. *Phys. Rev. Lett.* **107**, 158101 (2011).
53. Ducret, A., Quardokus, E. M. & Brun, Y. V. MicrobeJ, a tool for high throughput bacterial cell detection and quantitative analysis. *Nat. Microbiol.* **1**, 16077 (2016).
54. Reddy, C. A. et al. (eds) *Methods for General and Molecular Microbiology* (ASM Press, 2007).

Acknowledgements

We thank Tom Bernhard and Anastasiya Yakhnina for assorted *E. coli* strains, Ünal Coskun and Michal Grzybek for assistance with lipid analyses, and Allison J. Lopatkin, Ian W. Andrews, Emma J. Chory, Erica J. Zheng, and members of the Collins lab for helpful discussions and comments. F.W. was supported by the James S. McDonnell Foundation. J.M.S. was supported by the Banting Fellowships Program (393360). L.D.R. was supported by the Volkswagen Foundation. J.J.C. was supported by the Defense Threat Reduction Agency (grant number HDTRA1-15-1-0051), the National Institutes of Health (grant number R01-AI146194), and the Broad Institute of MIT and Harvard.

Author contributions

F.W. conceived research, performed experiments and analysis, developed the model, wrote the paper, and supervised research. J.M.S. provided assistance with data interpretation and manuscript editing. B.C. provided assistance with experiments. S.P. performed experiments. J.F. and L.D.R. conceived research and performed experiments and analysis. J.J.C. conceived and supervised research.

Competing interests

J.J.C. is scientific co-founder and scientific advisory board chair of EnBiotix, an antibiotic drug discovery company. The remaining authors declare no competing interests.

Additional information

Supplementary information The online version contains supplementary material available at <https://doi.org/10.1038/s41467-021-22485-6>.

Correspondence and requests for materials should be addressed to L.D.R. or J.J.C.

Peer review information *Nature Communications* thanks David Alsteens, Matthias Koch and the other, anonymous, reviewers for their contribution to the peer review of this work. Peer reviewer reports are available.

Reprints and permission information is available at <http://www.nature.com/reprints>

Publisher's note Springer Nature remains neutral with regard to jurisdictional claims in published maps and institutional affiliations.



Open Access This article is licensed under a Creative Commons Attribution 4.0 International License, which permits use, sharing, adaptation, distribution and reproduction in any medium or format, as long as you give appropriate credit to the original author(s) and the source, provide a link to the Creative Commons license, and indicate if changes were made. The images or other third party material in this article are included in the article's Creative Commons license, unless indicated otherwise in a credit line to the material. If material is not included in the article's Creative Commons license and your intended use is not permitted by statutory regulation or exceeds the permitted use, you will need to obtain permission directly from the copyright holder. To view a copy of this license, visit <http://creativecommons.org/licenses/by/4.0/>.

© The Author(s) 2021

Supplementary Information: Cytoplasmic condensation induced by membrane damage is associated with antibiotic lethality

Felix Wong^{1,2}, Jonathan M. Stokes^{1,2}, Bernardo Cervantes^{1,2,3}, Sider Penkov⁴, Jens Friedrichs⁵, Lars D. Renner^{5,*}, and James J. Collins^{1,2,6,*}

¹Institute for Medical Engineering & Science and Department of Biological Engineering, Massachusetts Institute of Technology, Cambridge, MA 02139, USA

²Infectious Disease and Microbiome Program, Broad Institute of MIT and Harvard, Cambridge, MA 02142, USA

³Microbiology Graduate Program, Massachusetts Institute of Technology, Cambridge, MA 02139, USA

⁴Institute for Clinical Chemistry and Laboratory Medicine at the University Clinic and Medical Faculty of TU Dresden, 01307 Dresden, Germany

⁵Leibniz Institute of Polymer Research and the Max Bergmann Center of Biomaterials, 01069 Dresden, Germany

⁶Wyss Institute for Biologically Inspired Engineering, Harvard University, Boston, MA 02115, USA

*Corresponding authors: James J. Collins (jimjc@mit.edu) and Lars D. Renner (renner@ipfdd.de)

Supplementary Note 1

1.1 Generality of observed phenotypes

Here, we discuss the generality of results presented in the main text. In brief, we find evidence for the accumulation of reactive metabolic byproducts, but did not observe cytoplasmic condensation, in cells treated by β -lactams (Supplementary Fig. 1). Furthermore, we observed cytoplasmic condensation across different aminoglycosides and quinolones and in a different, Gram-positive species, *B. subtilis* (Supplementary Fig. 3).

1.1.1 β -lactam antibiotics

In *E. coli* cells treated by ampicillin, we observed increased fluorescence of carboxy- H_2 DCFDA, DAF-FM, and C11-BODIPY relative to untreated controls (Supplementary Fig. 1c-e). However, we did not find significant cytoplasmic condensation in cells treated with either ampicillin or less lytic antibiotics such as mecillinam (Supplementary Fig. 1a,b), suggesting that typical cells likely undergo a different cell death pathway involving membrane bulging, as previous work has shown [1]. In contrast to kanamycin and ciprofloxacin, we found that ampicillin killing was less susceptible to glutathione protection (Supplementary Fig. 1f). A previous study [2] has shown that higher levels (50 mM) of glutathione pretreatment than those used in this work can better attenuate ampicillin killing, by as much as ~ 3 logs; together with our results, these observations suggest glutathione protection in β -lactams to be largely concentration- and antibiotic-dependent.

1.1.2 Cytoplasmic condensation across different aminoglycoside and quinolone antibiotics, and also in *Bacillus subtilis*

In addition to kanamycin (Supplementary Fig. 3a) and ciprofloxacin (Fig. 1b of the main text), we observed similar cytoplasmic condensation in gentamicin- (an aminoglycoside) and norfloxacin- (a quinolone) treated *E. coli* (Supplementary Fig. 3b). The evolutionarily distant, Gram-positive rod *B. subtilis* also exhibited similar condensation and lysis and increased levels of lipid peroxidation, as assayed by C11-BODIPY, when treated with kanamycin and ciprofloxacin (Supplementary Fig. 3c). Intriguingly, the incidence of cytoplasmic condensation in *B. subtilis* was decreased relative to *E. coli* under both kanamycin and ciprofloxacin treatment. Furthermore, we observed significant membrane bulging in *B. subtilis* cells treated by ciprofloxacin (Supplementary Fig. 3c), reminiscent of bulging *E. coli* cells treated by β -lactams [1, 3]. The occurrence of membrane bulging in *B. subtilis* is surprising, since its turgor pressure is estimated to be ~ 10 -fold larger than that of *E. coli* [4], while the yield areal strains of bacterial membranes are anticipated to be similar [1, 5]. Thus, if the mechanical stresses in a membrane bulge were $pR/2$, where p is the turgor pressure and R is the radius of the bulge [1], then we would anticipate *B. subtilis* cells to lyse immediately after bulge formation due to membrane yielding. The occurrence of bulging in *B. subtilis* therefore suggests that, like *E. coli* (below), *B. subtilis* cells may also lose a significant amount of cellular turgor due to membrane damage as a result of ciprofloxacin treatment.

1.1.3 Relation to previous work

As a historical remark, we note that aspects of cytoplasmic condensation have been observed in previous work revealing the leakage of [3 H]-uracil-labeled cellular contents [6, 7] and formation of vacuoles [8] in quinolone-treated *E. coli*. However, to our knowledge, a physiological characterization of the condensed state, in addition to the relationship between condensation and turgor loss, cell death, reactive metabolic byproducts, and glutathione protection, has not, until now, been studied.

1.2 Biophysical model of cytoplasmic condensation

To better understand the physiology of the condensed state, we developed a biophysical model of cell envelope mechanics which predicts (1) smaller turgor and cytoplasmic condensation to arise from elastic relaxation to an equilibrium state, which is governed by flow of solutes outside the cell and induced by nanometer-scale membrane defects; and (2) the number of such defects consistent with the empirically

observed timescale and magnitude of condensation. Building on previous work [1], we model the Gram-negative bacterial cell envelope as the combination of an elastic shell (the cell wall) sandwiched between two fluid membranes (the inner and outer membranes). The free energy of the cell envelope and its enclosed volume includes both the elastic strain energies of all three layers and the entropy of mixing, primarily of solutes contained within:

$$\mathcal{F} = E_{\text{strain}}^w + E_{\text{strain}}^i + E_{\text{strain}}^o - TS. \quad (\text{S1})$$

Here, the superscripts w , i , and o denote cell wall, inner membrane, and outer membrane quantities, respectively, E_{strain} is the elastic strain energy, T is the temperature, and S is the entropy of mixing water and solute molecules. For simplicity, we assume that there are only water molecules outside the cell; S can then be expressed as $S = -k(n_s \ln x_s + n_w \ln x_w)$, where k is Boltzmann's constant, x_s and x_w are the number fractions of solute and water molecules, respectively, and n_s and n_w are the numbers of solute and water molecules, respectively. We point out the following details regarding the model:

- The turgor pressure is defined as $p = kTC$, where C is the solute concentration. Note that the origin of turgor pressure is entropic, and it will therefore decrease continuously with flow of solutes outside the cell and flow of water into the cell (below).
- Throughout, we will neglect the hemispherical poles of the cell for simplicity and consider only the cylindrical bulk.
- We assume that the contributions of any disjoint, but potentially load-bearing cytoskeletal elements, such as MreB [9], are coarse-grained by the continuum description of the cell envelope layers above; the elastic moduli should therefore be viewed as effective ones.
- For simplicity, we will focus on modeling the cellular periplasm as, effectively, a rigid, permeable, and gel-like body that supports the inner membrane [10, 11, 12], but is not isosmotic with the cytoplasm [13]. A previous study combining diffusion measurements in the cytoplasm and periplasm and hyperosmotic shocks suggested that the periplasm is iso-osmotic with the cytoplasm, with the main turgor pressure drop occurring across the cell wall and outer membrane. However, as indicated by a subsequent study [11], in this case the bending energy of the inner membrane would be minimal for rod-like cells when the inner membrane assumes the shape of a cylinder with the largest radius possible. Equilibration of the inner membrane would therefore result in the inner membrane squeezing out the periplasm. A model in which the periplasm and cytoplasm are isosmotic, with no force exerted on the inner membrane by the periplasm, is therefore inconsistent with the existence of a periplasm. The periplasm may exist upon the inclusion of a membrane pinning potential [11, 12]; however, as noted before [11], for previously considered parameter values [12], the membrane pinning potential is large enough so that the periplasm is effectively a rigid body.
- Additionally, we assume that the periplasm does not hinder the transport of solutes and water out of the cytoplasm and can be viewed independently of each cell envelope component. We therefore neglect the periplasm in what follows.
- Finally, we note that, although molecules such as Braun's lipoprotein anchor the outer membrane to the cell wall, the estimated number of such outer membrane-wall anchors ($\sim 10^6$) are few in comparison to the estimated numbers ($\sim 10^7$) of phospholipids [1, 14, 15]. Hence, free phospholipids could modulate the reference membrane states and allow for membrane reorganization. That the cell envelope layers can slide with respect to each other will be relevant to the calculations in §1.2.2 below.

1.2.1 Change in cellular turgor and volume due to membrane defects

We hypothesize that membrane damage is well described by the appearance of nanoscale gaps in the membrane (Fig. 2a of the main text). Accordingly, we model membrane defects as holes with characteristic radius $r_d \approx 1$ nm, which is much smaller than the combined thickness of the inner and outer membranes, ~ 20 nm. Assuming it to be laminar, the hydrodynamic flow of cytoplasmic contents from inside to outside

the cell is well described by Poiseuille flow, with a volumetric flow rate of

$$Q = \frac{\Delta P A^2}{8\pi\mu L_d}. \quad (\text{S2})$$

Here ΔP is the pressure drop inside and outside the cell, $A = \pi r_d^2$ is the defect area, L_d is the defect length, and μ is the viscosity of the medium. Note that, due to the entropic origin of turgor, p decreases with flow of solutes outside the cell and flow of water into the cell through the semi-permeable cell membranes. In turn, the membrane defect radius will decrease with the turgor due to there being less mechanical strain in the cell membranes. Nonetheless, for characteristic parameter values, as summarized in Supplementary Table 2, we note that, at the start of flow, $Q \approx 10^{-21} \text{ m}^3/\text{s}$ and the Reynolds number is $\text{Re} = 2Qr_d\rho/(\mu A) \approx 10^{-6}$, where ρ is the density of water. This suggests, self-consistently, the flow to indeed be laminar. Furthermore, assuming this flow rate to be constant in time, a simple but surprising estimate shows that only ten such pores, corresponding to removal of only $\sim 0.0001\%$ of all phospholipids in a membrane layer, are sufficient to predict a flow comparable to the entire cellular volume out of the cell within one minute.

We now undertake a more detailed analysis, taking into account the decrease of turgor and defect radius with flow of solutes outside the cell. A characteristic value of the diffusion constant of ions in water is $D \approx 10^{-9} \text{ m}^2/\text{s}$ [16], so that a typical root-mean-square distance traveled by an ion per second is $10 \text{ }\mu\text{m}$. Accordingly, we assume solutes to be significantly diluted once outside the cell, so that $\Delta P = p$, the turgor pressure of the cell. Viewing n_s , p , r_d , Q , and the cell volume, V , as time-dependent quantities that change with flow of solutes out of the cell, we therefore write:

$$Q(t) = \frac{\pi p(t) r_d(t)^4}{8\mu L_d}, \quad p(t) = \frac{kT n_s(t)}{V(t)}, \quad \frac{dn_s(t)}{dt} = -\frac{\mathcal{N}Q(t)n_s(t)}{V(t)}, \quad (\text{S3})$$

where \mathcal{N} is the number of such membrane defects. It remains to determine $V(t)$ and $r_d(t)$; this becomes a problem of elasticity.

1.2.2 Elastic determination of the cellular volume

Due to the possibility of water flow into the membrane as the number of solutes are modulated, we hypothesize that the cellular volume is determined by the equilibration of the elastic strain energies in Eq. (S1). In particular, given the turgor pressure, $p(t)$, the cell envelope is free to change its dimensions to minimize the free energy. The bulk flow of water through the cell membranes is described by

$$\frac{dV_{\text{water}}}{dt} = L_p A_{\text{cell}} p, \quad (\text{S4})$$

where L_p is the hydraulic conductivity of the membranes and A_{cell} is the total membrane surface area [17]. For characteristic values of these parameters, as summarized in Supplementary Table 2, we find that a typical $\sim 40\%$ change in cellular volume occurs within $\sim 1 \text{ s}$. Hence, for the timescale of interest ($\sim 1 \text{ s}$) here, we find that water flow indeed occurs fast enough for the cell to be in equilibrium.

We therefore determine $V(t)$ and $r_d(t)$ by finding the elastic stresses in the equilibrium conformation. For this, we resort to a linear theory and assume a linear-elastic cell wall, with reference radius and lengths r_0^w and L_0^w , respectively, and (two-dimensional) Young's modulus and Poisson's ratio Y^w and ν^w , respectively. Moreover, we view the two membranes as materially identical and fluid in-plane, so that their stretching is governed by their area-stretch modulus, $K = K^i = K^o$, and excess reference surface area ratio, $\gamma = A_0^i/A_0^w - 1 = A_0^o/A_0^w - 1$, where A_0^w is the reference cell wall surface area, and A_0^i and A_0^o are the inner and outer membrane reference surface areas, respectively [1]. Ignoring bending terms, which are anticipated to be dominated by the stretching terms [1], the free energy of Eq. (S1) can then be expressed as

$$\mathcal{F} = \frac{1}{2Y^w} \int [(\sigma_{xx}^w)^2 + (\sigma_{yy}^w)^2 - 2\nu^w \sigma_{xx}^w \sigma_{yy}^w] dA^w + 2K \int (u^i)^2 dA^i + 2K \int (u^o)^2 dA^o - TS, \quad (\text{S5})$$

where the integrals are over the deformed surface areas, σ_{xx}^w and σ_{yy}^w are cell wall stresses, and u^i and u^o are inner and outer membrane strains, respectively. Note that the form of E_{strain}^i and E_{strain}^o in Eq. (S5) arises from the fluid in-plane nature of the membranes; it follows from this that the membrane strains and stresses are isotropic and spatially homogeneous [1]. As the cell wall is cylindrical, its strains and stresses will also be spatially homogeneous, but not necessarily isotropic.

Depending on the values of γ , K , and p , we note that the deformed membrane dimensions may be different from each other and those of the cell wall: in the limit of small $-1 < \gamma \ll 0$ and $p\ell/K \ll 1$ for a characteristic membrane length ℓ , for instance, the free energy is minimal when the inner membrane forms a spherical vesicle inside the cell and the cell wall and outer membrane bear no load. However, we may anticipate a parameter regime in which each envelope layer bears some load (below). Then, by symmetry of the inner and outer membranes, $u = u^i = u^o$ and the membrane stresses $\sigma = \sigma^i = \sigma^o$; moreover, these quantities will all be nonzero. In general, the mechanical stresses will be related to the strains by the following constitutive relations [1]:

$$\sigma_{xx}^w = \frac{Y^w}{1 - (\nu^w)^2} (u_{xx}^w + \nu^w u_{yy}^w), \quad \sigma_{yy}^w = \frac{Y^w}{1 - (\nu^w)^2} (u_{yy}^w + \nu^w u_{xx}^w), \quad \sigma = 2Ku. \quad (\text{S6})$$

Here, the cell wall strains u_{xx}^w and u_{yy}^w correspond to the stresses σ_{xx}^w and σ_{yy}^w . Furthermore, the linear strain-displacement relations are

$$u_{xx}^w = \frac{r - r_0^w}{r_0^w}, \quad u_{yy}^w = \frac{L - L_0^w}{L_0^w}, \quad u = \frac{A^i - A_0^i}{2A_0^i} = \frac{A^o - A_0^o}{2A_0^o}, \quad (\text{S7})$$

where r and L are the deformed cell wall radius and length, respectively. Assuming that the membranes share the same deformed radius and length (below), we substitute Eqs. (S6) and (S7), as well as the relation $n_w = \pi r^2 L / m_w$, where m_w is the volume occupied per water molecule, into Eq. (S5). From this, we find that \mathcal{F} can be rewritten as a function of two unknowns, r and L , and several parameters including the elastic constants, γ , and n_s . Hence, we will minimize \mathcal{F} over r and L , from we determine all associated elastic quantities.

As mentioned above, we anticipate that, for typical cells, the membrane reference areas will be similar to that of the cell wall, so that $|\gamma| \ll 1$ [1]. Furthermore, we anticipate all cell envelope layers to be load-bearing and in contact in the deformed state, so that we may suppose a common value of the deformed cell length and radius among all envelope layers; these may be expressed as $L = L_0^w + \delta L$ and $r = r_0^w + \delta r$, where δL and δr are viewed as small relative to L_0^w and r_0^w . Next, we make the following small-variable assumptions: $n_s/n_w \ll 1$ and $\delta r/r, \delta L/L = O(\varepsilon)$, where $\varepsilon \ll 1$, consistent with the linear theory. In particular, we will expand \mathcal{F} to first order in γ , first order in n_s , and second order in ε . Doing so, and analytically solving for the values of δL and δr which minimize \mathcal{F} , upon substitution of the solution into Eqs. (S6) and (S7) we find

$$\sigma_{xx}^w = \frac{\gamma KY^w}{Y^w + 2K(1 - \nu^w)} + \frac{kTn_s[K(1 - \nu^w) + 2Y^w]}{2\pi r_0^w L_0^w [2K(1 - \nu^w) + Y^w]} \quad (\text{S8})$$

$$+ O(\varepsilon^2) + O\left[\left(\frac{n_s}{n_w}\right)^2\right] + O(\gamma^2) + O(\gamma\varepsilon) + O\left(\frac{\gamma n_s}{n_w}\right) + O\left(\frac{\varepsilon n_s}{n_w}\right).$$

Accurate to the same order, we have

$$\sigma_{yy}^w = \frac{\gamma KY^w}{Y^w + 2K(1 - \nu^w)} + \frac{kTn_s[K(1 - (\nu^w)^2) + Y^w]}{2\pi r_0^w L_0^w [2K(1 - \nu^w) + Y^w]}, \quad \sigma = \frac{K[3kTn_s(1 - \nu^w) - 2\pi r_0^w L_0^w \gamma Y^w]}{4\pi r_0^w L_0^w [2K(1 - \nu^w) + Y^w]}. \quad (\text{S9})$$

It is straightforward to verify that $\sigma_{xx}^w + 2\sigma = \frac{kTn_s}{\pi r_0 L_0}$ and $\sigma_{yy}^w + 2\sigma = \frac{kTn_s}{2\pi r_0 L_0}$, so that Laplace's law [1] is satisfied. Furthermore, when $K = 0$, the membrane stress $\sigma = 0$ and we recover the cylinder stresses $\sigma_{xx}^w = \frac{kTn_s}{\pi r_0 L_0}$ and $\sigma_{yy}^w = \frac{kTn_s}{2\pi r_0 L_0}$ in the cell wall.

Finally, by viewing the stresses in Eqs. (S8) and (S9) as functions of time through their dependence on $n_s = n_s(t)$ and finding the corresponding time-dependent strains through the linear constitutive relations of Eq. (S6), we can write closed-form expressions for the following:

$$V(t) = \pi(r_0^w)^2 L_0^w [1 + 2u_{xx}^w(t) + u_{yy}^w(t)], \quad r_d(t) = r_d^0(1 + u(t)). \quad (\text{S10})$$

Here r_d^0 denotes the reference (unstretched) radius of the membrane defect, and henceforth all equalities will be accurate to the orders shown in Eq. (S8).

1.2.3 The final dynamical equation

Iteratively substituting Eqs. (S6)-(S10) into Eq. (S3), we find that a single equation governs the dynamics of solute flow which, in turn, determines all other quantities:

$$\frac{dn_s(t)}{dt} = - \frac{\mathcal{N}kTn_s(t)^2(Y^w)^2[2\pi r_0^w L_0^w r_d^0(8K(1-\nu^w) + (4-\gamma)Y^w) + 3kTr_d^0(1-\nu^w)n_s(t)]^4}{\Phi(t)}, \quad (\text{S11})$$

where $\Phi(t) = 8192\pi^3\mu L_d(r_0^w)^6(L_0^w)^4[2K(1-\nu^w)+Y^w]^2[2\pi r_0^w L_0^w Y^w(K(2+3\gamma)(1-\nu^w)+Y^w)+kTn_s(t)(K(1-\nu^w)^2+(5-4\nu^w)Y^w)]^2$, and $n_s(t=0) = n_s^0$, the initial number of solutes inside the cell. This is a complicated ordinary differential equation involving a degree-six rational function that is difficult to solve analytically or approximately for the parameter values of interest. We therefore turn to numerical solutions of this equation for these parameter values (Supplementary Table 2).

1.2.4 The equilibrium state: timescales of equilibration and cellular morphology

Solving the dynamical Eq. (S11) numerically for the parameter values summarized in Supplementary Table 2, we find that the model predicts a cellular volume shrinkage of $\sim 20\%$ over the empirically observed, minute-timescale of condensation, consistent with experimental observations (Fig. 2b-f of the main text). For this to occur, the model shows that the turgor pressure is essentially abolished on the minute timescale (Fig. 2e of the main text), consistent with our osmotic shock experiments (Fig. 1e of the main text and Supplementary Fig. 5). Furthermore, the model predicts that the condensed state is not only a state of mechanical equilibrium, but also a steady state ($t \rightarrow \infty$) maintained by increasingly small solute leakage and cellular volume shrinkage (Fig. 2d,f of the main text). Indeed, the model predicts that there remains cytoplasmic material in condensed cells. This is consistent with fluorescence microscopy (Fig. 1b of the main text) and AFM measurements, which show the elastic moduli of a typical condensed cytoplasm to be larger than that of the shrunken region (Fig. 1f of the main text and Supplementary Fig. 7). We note here that these model predictions are general across a range of different membrane defect sizes and, for different defect sizes, predict different numbers of membrane defects to form (Supplementary Fig. 10).

For $\gamma < 0$ and vanishingly small turgor pressures corresponding to large t (Fig. 2e of the main text), we note that the inner membrane may form invaginations and retract from the cell wall, consistent with Fig. 1b of the main text. In this case, the assumption that all envelope layers are load-bearing no longer holds. The accuracy of the model at long times therefore depends on γ ; nonetheless, for $\gamma \approx 0$, as may be expected for *E. coli* [1], we expect the model to be accurate and robust at the onset of condensation, at which point all envelope layers are in contact and load-bearing.

Finally, we note that, in Eq. (S5) the mixing of solutes and water inside the cell is assumed to be homogeneous, and the free energy depends on the cell wall stresses, the cell wall area, the cell membrane areas, and the cellular volume. Consistent with ignoring bending terms in this expression, it is possible that the cell membranes may assume different shapes, provided that the remaining quantities are conserved. Accordingly, the model does not discriminate between condensed phenotypes wherein the phase-light region appears mid-cell or at the poles, and whether phase-dark regions of condensed cells may be connected. We anticipate future experimental studies to determine the factors that determine where, along a cell, condensation is initiated.

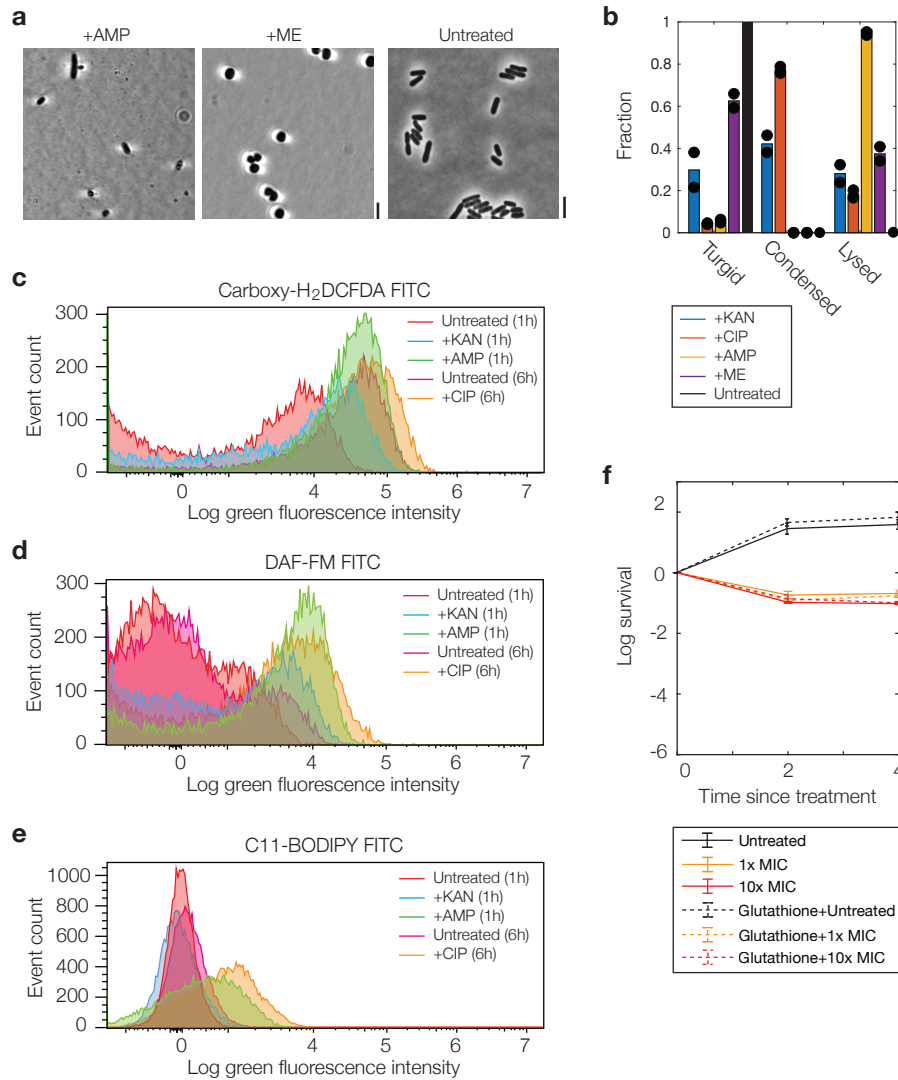
Supplementary Tables

Antibiotic	Empirical MIC Range ($\mu\text{g}/\text{mL}$)	Working MIC ($\mu\text{g}/\text{mL}$)
Kanamycin	<i>E. coli</i> MG1655: [5.0,12.0]	5.0
Ciprofloxacin	<i>E. coli</i> BW25113: [5.0,6.25]	0.1
	<i>E. coli</i> MG1655: [0.03125,0.125]	
	<i>E. coli</i> BW25113: [0.03125,0.125]	
	<i>E. coli</i> ΔgshA : [0.03125,0.125]	
Gentamicin	<i>E. coli</i> Δgor : [0.03125,0.125]	5.0
	<i>E. coli</i> MG1655: [3.13,6.25]	
	<i>E. coli</i> BW25113: [3.13,6.25]	
	<i>E. coli</i> ΔgshA : [3.13,6.25]	
Norfloxacin	<i>E. coli</i> Δgor : [3.13,12.5]	0.5
	<i>E. coli</i> MG1655: [0.15,0.5]	
Ampicillin	<i>E. coli</i> MG1655: [3.13,12.5]	10.0
	<i>E. coli</i> BW25113: [3.13,12.5]	
	<i>E. coli</i> ΔgshA : [3.13,12.5]	
	<i>E. coli</i> Δgor : [3.13,12.5]	
Mecillinam	<i>E. coli</i> MG1655: [0.63,2.0]	1.0
With 10 mM glutathione		
Kanamycin	<i>E. coli</i> MG1655: [39.0,78.0]	40.0
Ciprofloxacin	<i>E. coli</i> MG1655: [0.156,0.3125]	0.3
With 10 mM dithiothreitol		
Kanamycin	<i>E. coli</i> MG1655: [5.0,12.5]	5.0
Ciprofloxacin	<i>E. coli</i> MG1655: [0.03125,0.1]	0.1
With 10 mM mercaptoethanol		
Kanamycin	<i>E. coli</i> MG1655: [5.0,12.5]	5.0
Ciprofloxacin	<i>E. coli</i> MG1655: [0.03125,0.1]	0.1
With 50 mM α-tocopherol		
Kanamycin	<i>E. coli</i> MG1655: [5.0,12.5]	5.0
Ciprofloxacin	<i>E. coli</i> MG1655: [0.03125,0.1]	0.1

Supplementary Table 1: **Minimal inhibitory concentrations (MICs) of antibiotics used in this study.** Ranges were determined from three replicates for each culture dilution (1:100 and 1:10,000) and each growth vessel (14-mL Falcon tubes and 96-well plates); see *Methods* for details. Identical working MICs were used across all strains due to the similarity in observed empirical MIC ranges. Similar empirical MICs were observed, and the same working MICs for *E. coli* MG1655 used, for *B. subtilis* 168.

Variable	Value	Reference
Viscosity of water, μ	$8.9 \times 10^{-4} \text{ Pa} \cdot \text{s}$	–
Density of water, ρ	997 kg/m^3	–
Volume occupied per water molecule, m_w	$3 \times 10^{-29} \text{ m}^3$	–
Temperature, T	300 K	This work
Characteristic (reference) membrane defect radius, r_d^0	1 nm	This work
Characteristic membrane defect length, L_d	20 nm	This work
Characteristic number of membrane defects, \mathcal{N}	10	This work
Membrane bilayer thickness	10 nm	[18]
Membrane hydraulic conductivity, L_p	$10^{-12} \text{ m}^3/\text{N} \cdot \text{s}$	[17, 19]
Characteristic <i>E. coli</i> (reference) cell wall radius, r_0^w	$0.5 \mu\text{m}$	This work
Characteristic <i>E. coli</i> (reference) cell wall length, L_0^w	$2 \mu\text{m}$	This work
<i>E. coli</i> cell wall two-dimensional Young's modulus, Y^w	0.2 N/m	[1, 20, 21, 22]
<i>E. coli</i> cell wall Poisson's ratio, ν^w	0.2	[1, 22]
<i>E. coli</i> membrane area-stretch modulus, K	0.1 N/m	[1, 5]
<i>E. coli</i> membrane excess reference surface area ratio, γ	0	This work; estimate from [1]
<i>E. coli</i> (initial) turgor pressure, p	10^5 Pa	[1, 20, 23]
<i>E. coli</i> (initial) number of solutes, n_s^0	3.8×10^7	$p = kTn_s/[\pi(r_0^w)^2L_0^w]$

Supplementary Table 2: **Biophysical model parameters.**



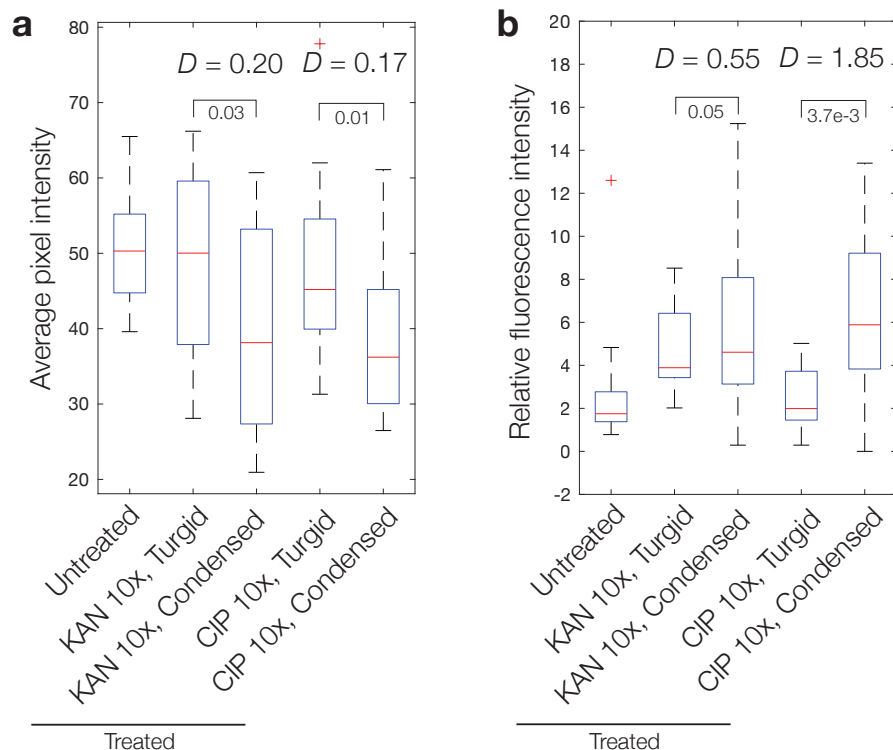
Supplementary Figure 1: Generality of results to β -lactam antibiotics.

a, Phase contrast microscopy images of *E. coli* cells treated by the β -lactam antibiotics ampicillin (AMP; left) and mecillinam (ME; right) 1 h after treatment, along with untreated control cells. Here and below, 10x MIC was used for all antibiotics, and scale bars indicate 3 μ m.

b, Frequency of condensation and lysis observed under β -lactam treatment, compared to kanamycin, ciprofloxacin and an untreated control, after 6 h. Data are from two different fields of view from two biological replicates, and individual datapoints corresponding to each field of view are shown. Bars indicate averages. Number of cells in each field of view: kanamycin, 105 and 93; ciprofloxacin, 241 and 198; ampicillin, 21, 32, and 35; mecillinam, 91 and 98.

c-e, Histograms of fluorescence intensities of populations of control and antibiotic-treated cells, as assayed by flow cytometry using the fluorochromes indicated, in the presence of carboxy- H_2 DCFDA, DAF-FM, and C11-BODIPY. Antibiotic-treated cells were treated for 1 h (ampicillin, kanamycin) or 6 h (ciprofloxacin); as in the main text, a longer treatment time was chosen for ciprofloxacin due to a majority of condensation events occurring later after treatment. Data representative of four biological replicates and 20,000 scattering events for each distribution.

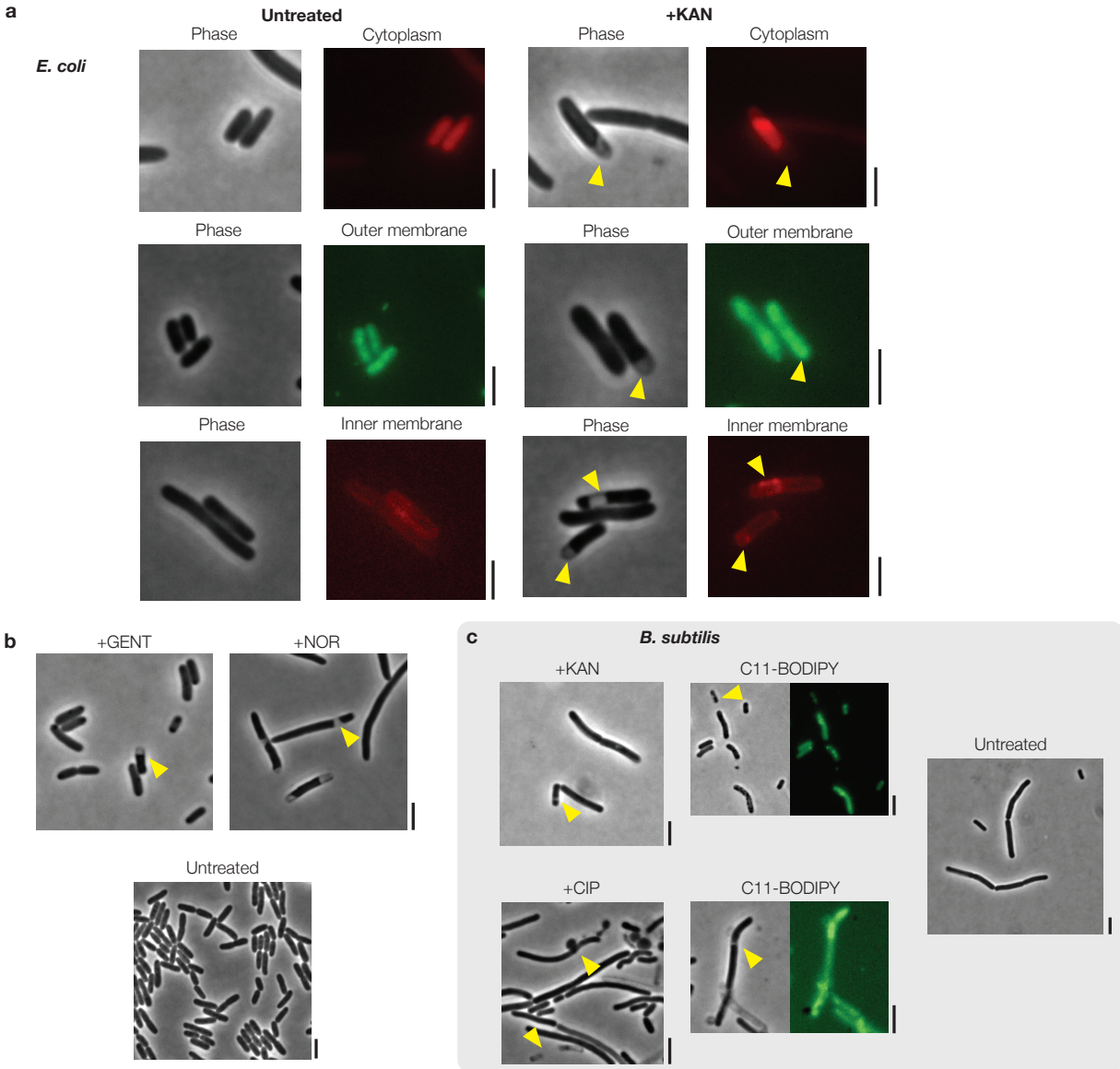
f, Survival curves under ampicillin treatment with and without exogenous supplementation of 10 mM glutathione, as determined by CFU measurements, at 1x and 10x MIC. Control experiments are also shown. Each point represents two biological replicates, error bars indicate one standard deviation, and data are presented as mean values \pm SEM.



Supplementary Figure 2: Phase contrast measurements of condensation indicate increased cytoplasmic density in condensed cells.

a, Quantitative comparison of average pixel intensities before and after cytoplasmic condensation for *E. coli* cells treated by kanamycin (10x MIC) and ciprofloxacin (10x MIC), along with control cells. Data are representative of three different fields of view with 20 cells in each group. D denotes the population-average relative decrease in the average pixel intensity of a cell. Here and below, box plots indicating the median (center), 25th percentile and 75th percentile (bounds of box), and extreme data points not considered outliers (bounds of whiskers) are shown, and red crosses indicate outliers including the minimum and maximum values. p -values for one-sample t -tests for the decrease in the average pixel intensity are shown next to corresponding brackets.

b, Same as **a**, but for relative fluorescence intensities in the cytoplasmic mCherry strain.

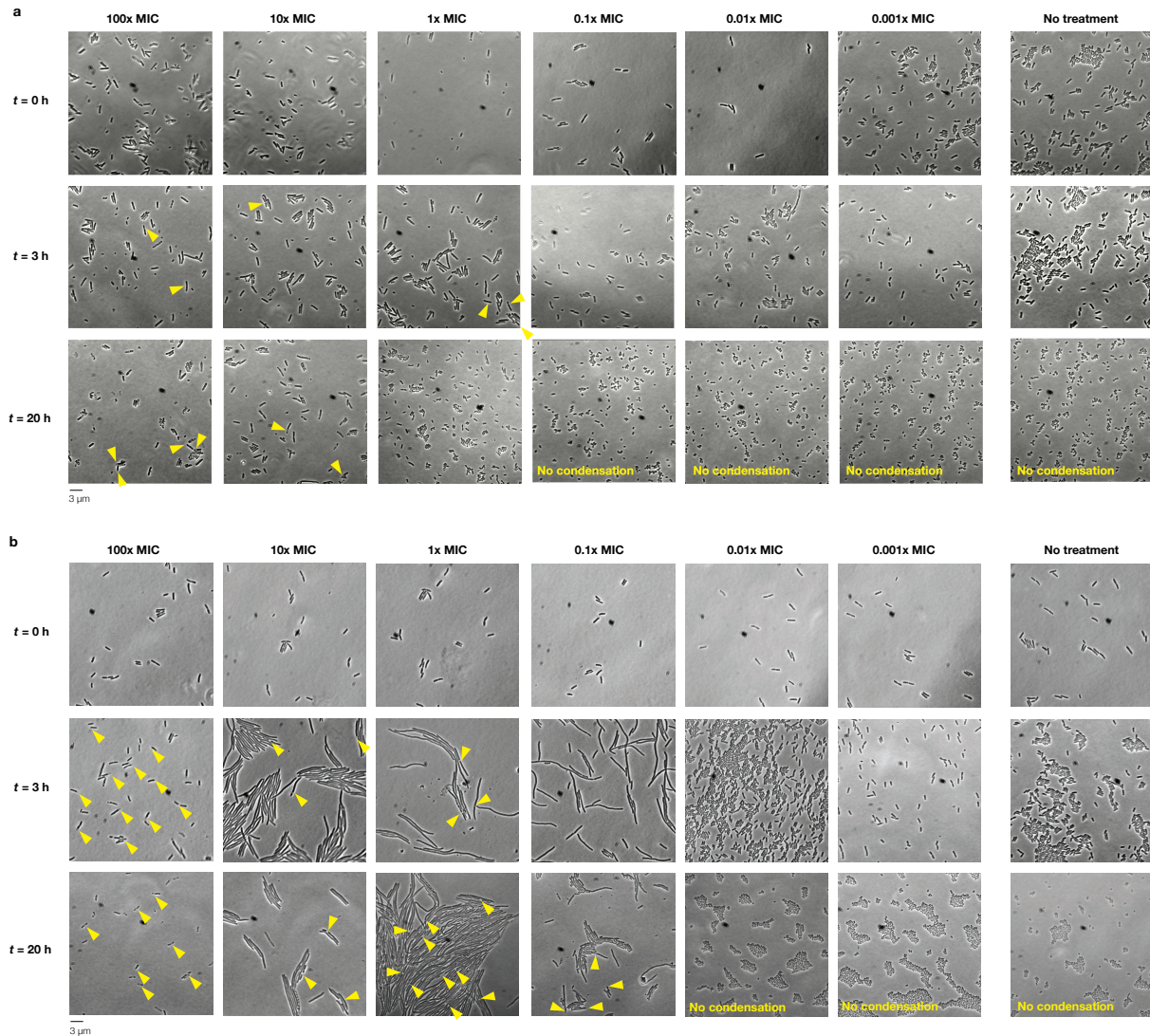


Supplementary Figure 3: **Generality of observed phenotypes to different antibiotics and bacterial species.**

a, *E. coli* cells with fluorescent cytoplasmic (mCherry), outer membrane (GFP), and inner membrane (mCherry) markers, as described in the *Methods*, with and without kanamycin treatment for 2 h at 10x MIC. Here and below, scale bars indicate 3 μm , imaging was performed in phase contrast and epifluorescence, and results are representative of two biological replicates. Yellow markers highlight condensed cells.

b, *E. coli* cells treated with other antibiotics for 2 h at 10x MIC: gentamicin (GENT), an aminoglycoside, and norfloxacin (NOR), a quinolone. Results are representative of two biological replicates, and yellow markers highlight condensed cells. A phase contrast microscopy image of corresponding untreated control cells is shown.

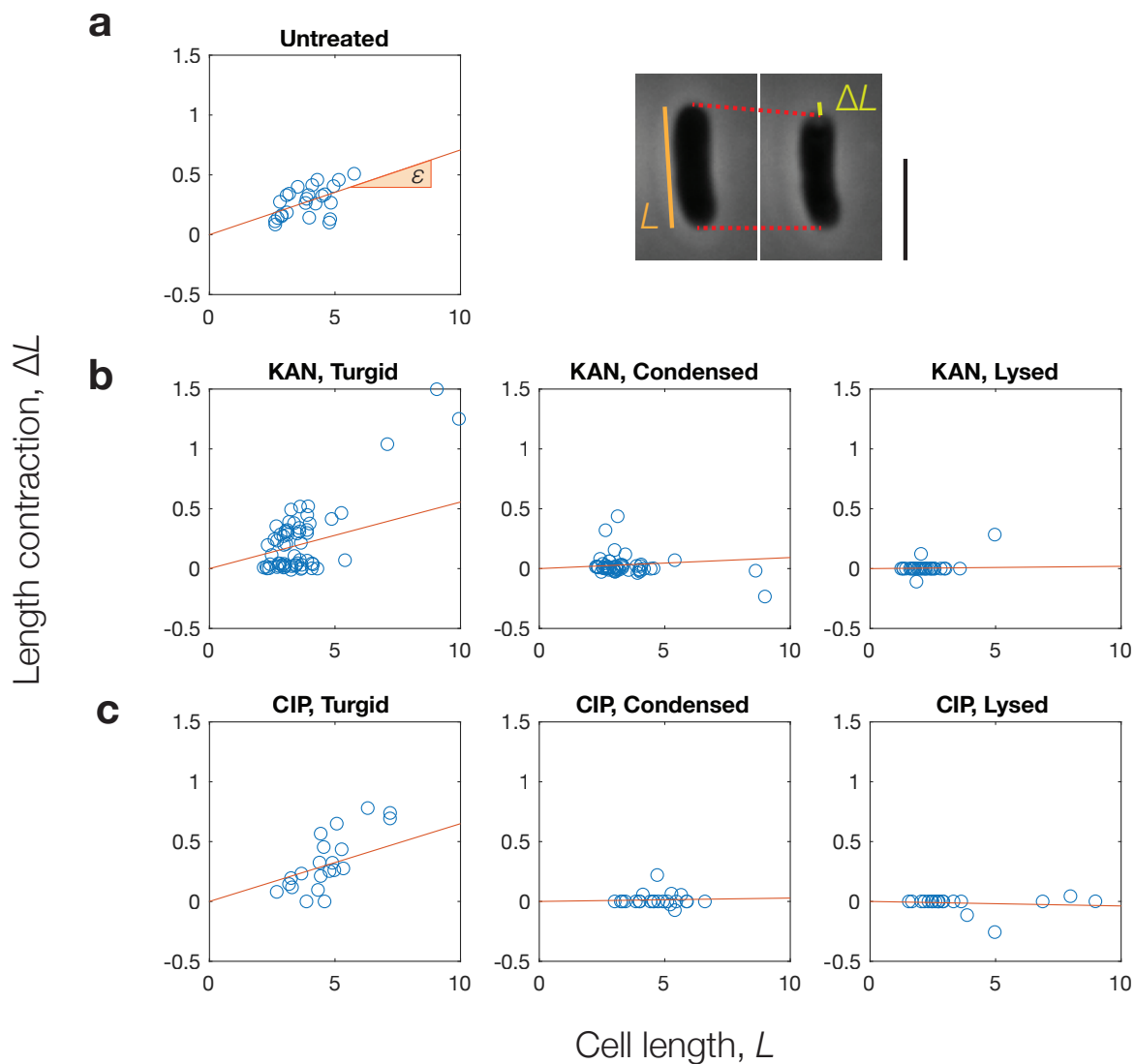
c, *B. subtilis* cells treated with kanamycin (50 $\mu\text{g}/\text{mL}$) and ciprofloxacin (1.0 $\mu\text{g}/\text{mL}$) after 2 h, with (right) and without (left) the dye C11-BODIPY. Results are representative of two biological replicates, and yellow markers highlight condensed, bulged, or lysed cells. A phase contrast microscopy image of corresponding untreated control cells is shown.



Supplementary Figure 4: Generality of the condensation phenotype across different antibiotic concentrations.

a, Phase contrast microscopy images of *E. coli* cells treated by various concentrations of kanamycin in culture as indicated, for various treatment times as indicated before imaging. Here time 0 refers to immediately before treatment. Each image is representative of three biological replicates, and yellow markers indicate a subset of condensed cells.

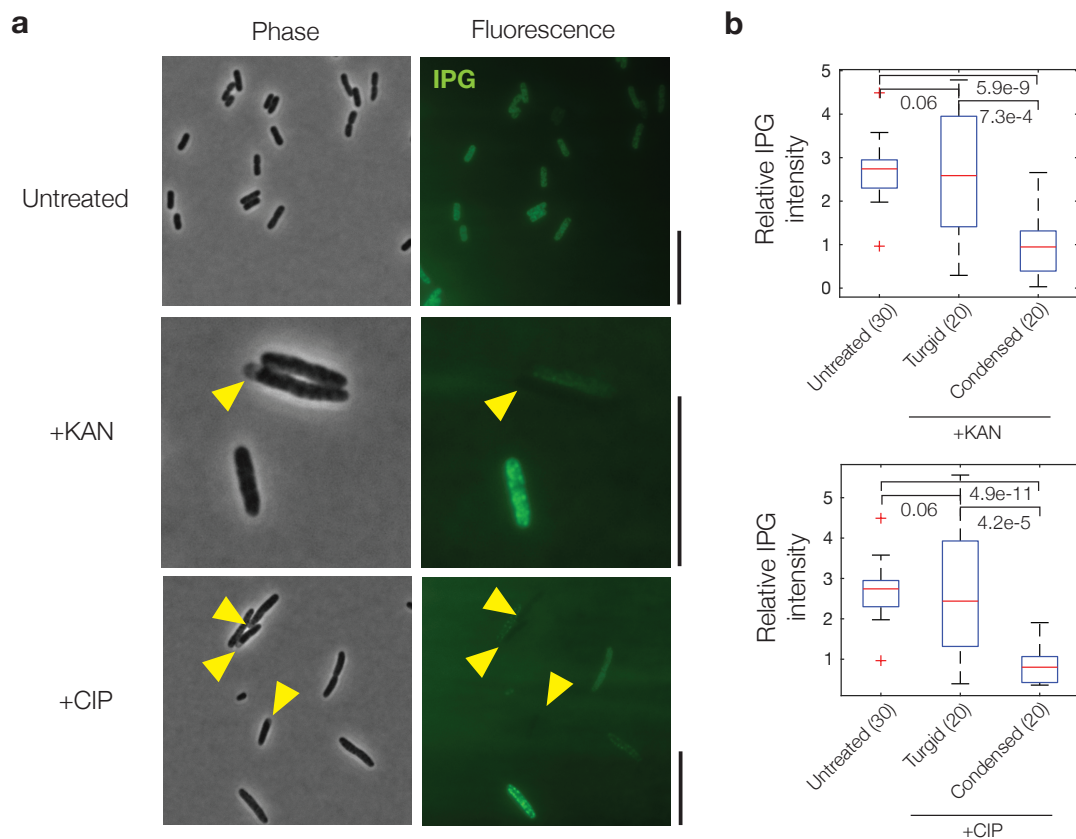
b, Same as panel **a**, but for ciprofloxacin.



Supplementary Figure 5: **Osmotic shocks reveal collapse of cellular turgor.**

a, Plot of pre-shock cell length against post-shock length contraction for the osmotic shock experiments summarized in Fig. 1e of the main text, showing approximately linear relationships. Control cells with no antibiotic treatment were used. The average percentage length contraction, or strain, ϵ , is the slope of the best fit line. (Right) Representative phase contrast microscopy images show the response of an untreated cell. Scale bar, $3 \mu\text{m}$.

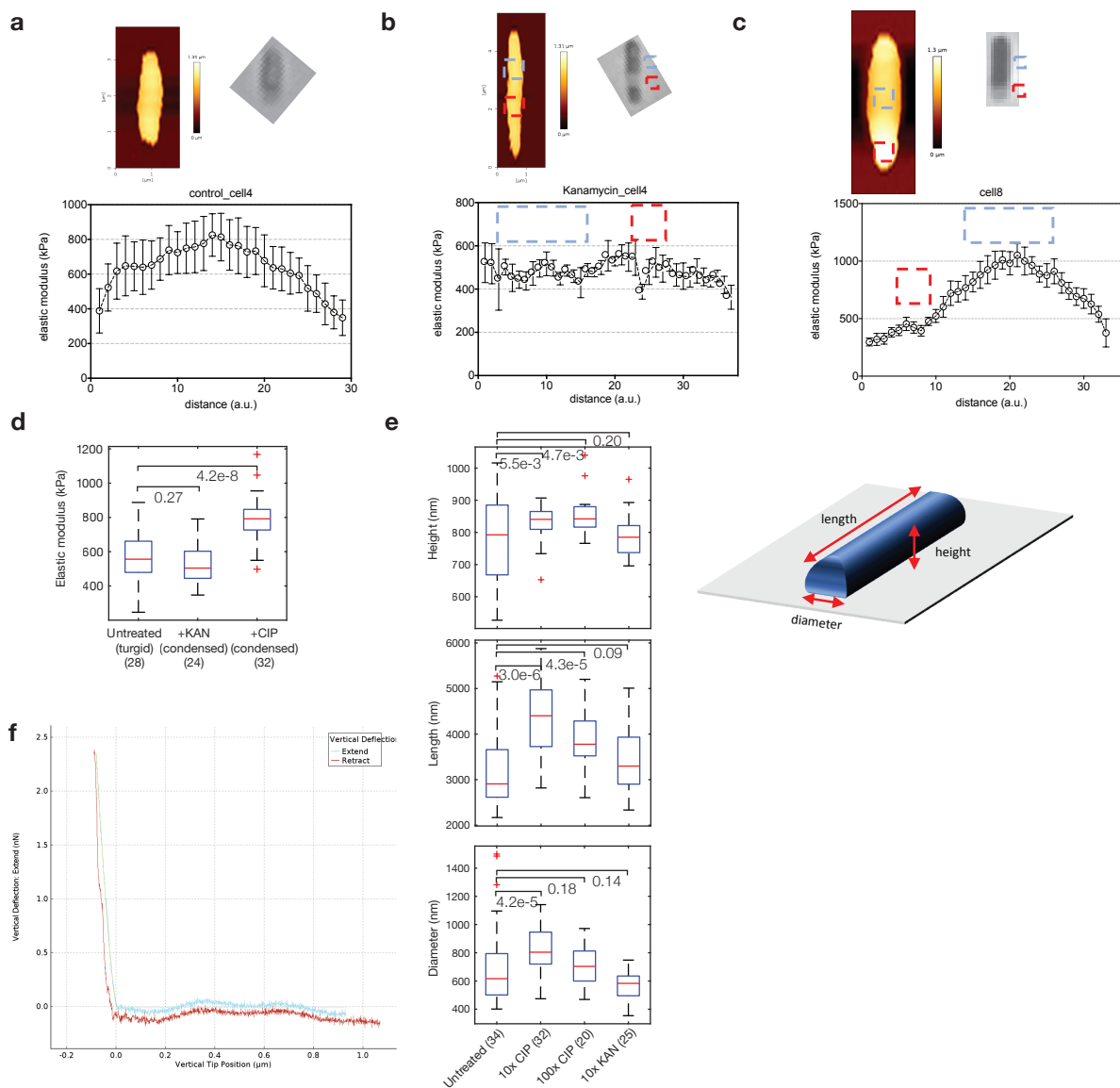
b-c, Same as panel **a**, but for cells treated by kanamycin (10x MIC; **b**) or ciprofloxacin (10x MIC; **c**) and classified by phenotype.



Supplementary Figure 6: **Measurements of IPG fluorescence.**

a, Phase-contrast and fluorescence microscopy images of control and antibiotic-treated cells (10x MIC) in the presence of IPG, a membrane-permeable potassium-sensitive dye. Cells were imaged at a time corresponding to 3 h of antibiotic treatment. Results are representative of two biological replicates, and yellow markers highlight condensed cells. Scale bars, 10 μ m.

b, Fluorescence intensities of control and antibiotic-treated cells in the presence of IPG. Box plots indicating the median (center), 25th percentile and 75th percentile (bounds of box), and extreme data points not considered outliers (bounds of whiskers) are shown, and red crosses indicate outliers including the minimum and maximum values. The numbers of cells in each group are indicated in parentheses, and *p*-values for two-sample Kolmogorov-Smirnov tests are shown next to corresponding brackets.



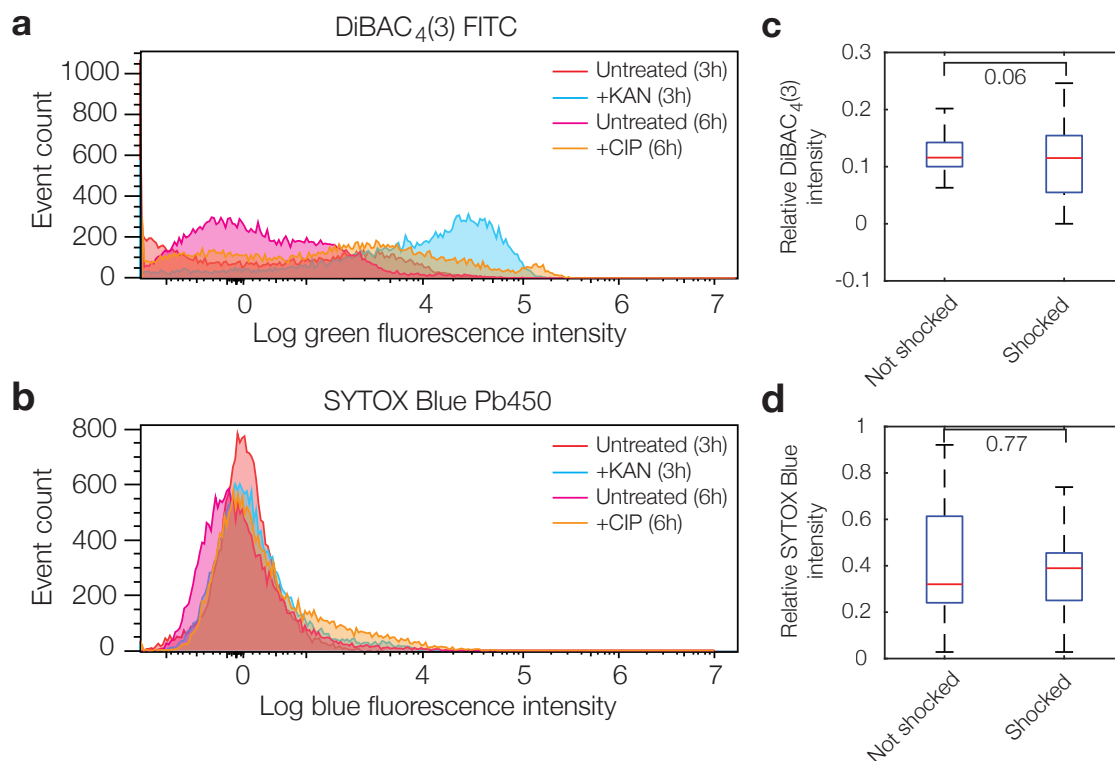
Supplementary Figure 7: Details of the AFM experiments.

a-c, Heatmaps of cell height (top) and plots of the elastic modulus (bottom) along the length of a cell (a.u.), for a representative untreated cell (**a**), a kanamycin-treated cell (10x MIC; **b**), and a ciprofloxacin-treated cell (10x MIC; **c**). Cells were assayed corresponding to a time ~ 3 h of antibiotic treatment. Error bars indicate one standard deviation from at least two technical replicates for the same cell, and data are presented as mean values \pm SEM. Colored boxes highlight cellular regions.

d, Comparison of cell-averaged elastic moduli across different treatment conditions (10x MIC). Here and below, box plots indicating the median (center), 25th percentile and 75th percentile (bounds of box), and extreme data points not considered outliers (bounds of whiskers) are shown, and red crosses indicate outliers including the minimum and maximum values. The numbers of cells in each group are indicated in parentheses, and p -values for two-sample Kolmogorov-Smirnov tests are shown next to corresponding brackets.

e, (Left) Similar to **d**, but for inferred cellular dimensions across different treatment conditions (10x MIC). (Right) Schematic of the different cellular dimensions measured.

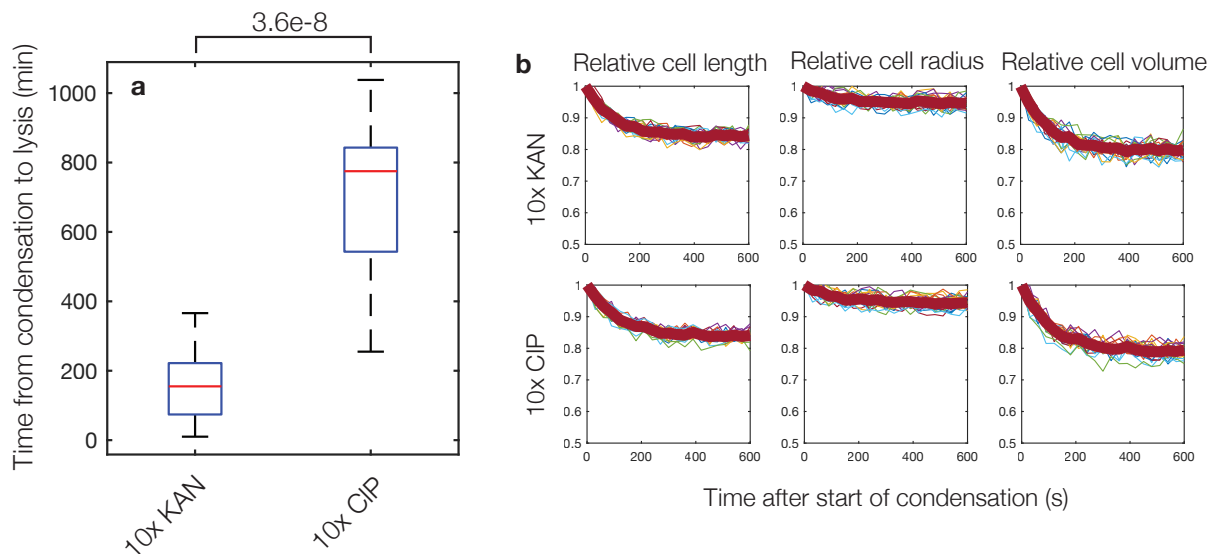
f, Sample force-distance curves from untreated control cells.



Supplementary Figure 8: **Additional DiBAC₄(3) and SYTOX Blue measurements.**

a-b, Histograms of fluorescence intensities of populations of control and antibiotic-treated cells in the presence of DiBAC₄(3) (**a**) and SYTOX Blue (**b**) 3 h after treatment (kanamycin) and 6 h after treatment (ciprofloxacin); as in the main text, a longer treatment time was chosen for ciprofloxacin due to a majority of condensation events occurring later after treatment. Concentrations used were 10x MIC for both antibiotics. Data representative of four biological replicates and 20,000 scattering events for each distribution. The fluorochromes used (FITC and Pb450) are indicated.

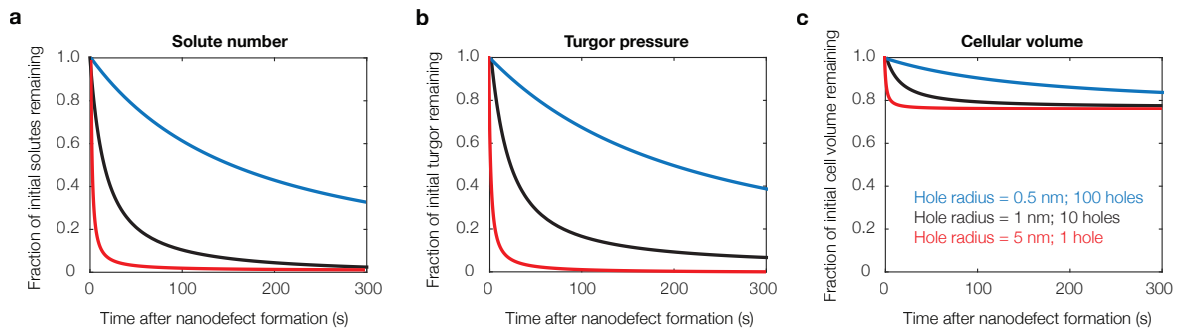
c-d, Fluorescence intensities of hyperosmotically shocked (500 mM sorbitol) cells in the presence of SYTOX Blue (**c**) and DiBAC₄(3) (**d**). Fluorescence images were taken immediately after shock. Data are from 20 cells in each group. Box plots indicating the median (center), 25th percentile and 75th percentile (bounds of box), and extreme data points not considered outliers (bounds of whiskers) are shown, and red crosses indicate outliers including the minimum and maximum values. *p*-values for two-sample Kolmogorov-Smirnov tests are shown next to corresponding brackets.



Supplementary Figure 9: **Times from condensation to lysis in antibiotic-treated cells and cellular dimensions of condensed cells.**

a, Times from condensation to lysis in kanamycin and ciprofloxacin-treated cells (10x MIC). Data are from 20 cells in each group. Box plots indicating the median (center), 25th percentile and 75th percentile (bounds of box), and extreme data points not considered outliers (bounds of whiskers) are shown, and red crosses indicate outliers including the minimum and maximum values. The p -value for a two-sample Kolmogorov-Smirnov test is shown next to the corresponding bracket.

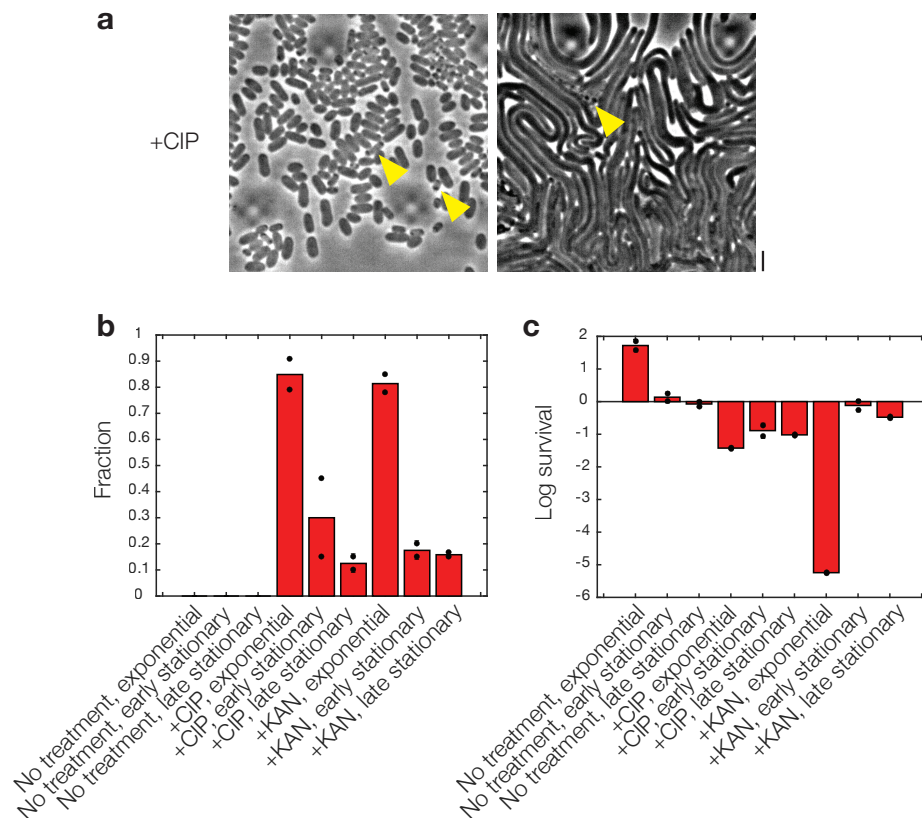
b, Changes in relative cell length, cell radius, and cell volume across time, from the beginning of condensation events, in kanamycin and ciprofloxacin-treated cells (10x MIC), corresponding to Fig. 2f in the main text. Data are from 20 cells in each group (colored curves), and population-averaged traces (thick red curves) are shown. Note that fluctuations in individual traces arise due to variations in semi-automated image processing; see *Methods* for details of the image analysis.



Supplementary Figure 10: **Sensitivity analysis of the model of solute outflow.**

a, Model predictions for the solute number as a function of time across different membrane defect radii (different colors). Depending on the size of typical membrane defect (0.5 nm, 1 nm, 5 nm radius), the model suggests that different numbers of membrane defects form (100, 10, and 1, respectively) as to be consistent with the minute-timescale of condensation. In all cases, the model predicts cells to condense after outflow of solutes from a cell, as detailed in Supplementary Note 1.

b-c, Same as panel **a**, but for the predicted cellular turgor pressure (**b**) and volume (**c**).

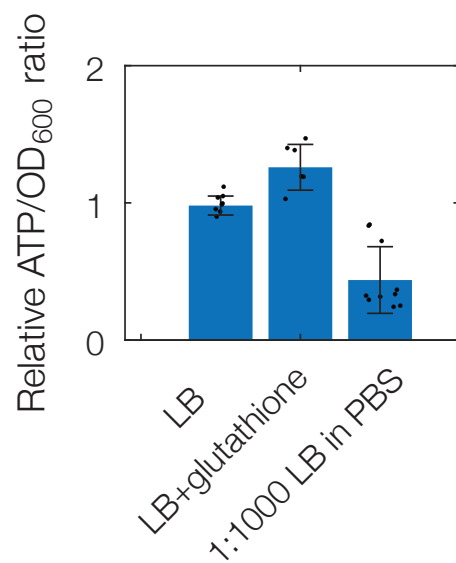


Supplementary Figure 11: Experiments on stationary-phase cells.

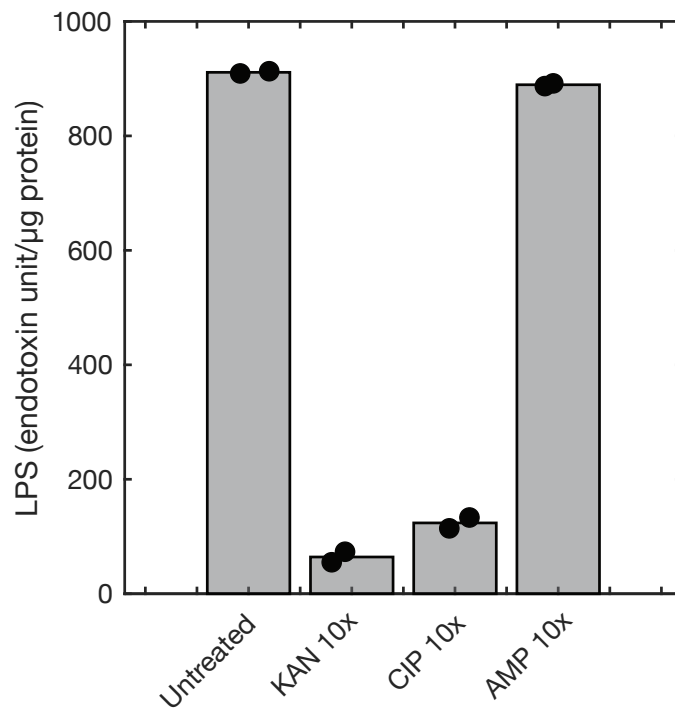
a, Microscopy images of early stationary-phase ($OD_{600} \approx 1.5$) *E. coli* cells treated by ciprofloxacin (10x MIC) at times 0 h (left) and 6 h (right). Results are representative of two biological replicates, and yellow markers indicate condensed or lysed cells. Scale bar, 3 μm .

b, Fractions of all cells that are condensed or lysed corresponding to the experiments in panel **a**, from two different fields of view of two biological replicates with at least 20 cells each, in addition to cells from early exponential phase ($OD_{600} \approx 0.1$) and late stationary phase ($OD_{600} > 2.0$), as described in the *Methods*. All antibiotics refer to 10x MIC, and “no treatment” cells were not treated by antibiotics. Individual points corresponding to each field of view are shown. The numbers of cells in each of two fields of view, according to the order of treatment shown along the horizontal axis, was as follows: 24 and 30, 56 and 76, 101 and 94, 195 and 206, 20 and 20, 20 and 20, 95 and 107, 20 and 20, 20 and 30.

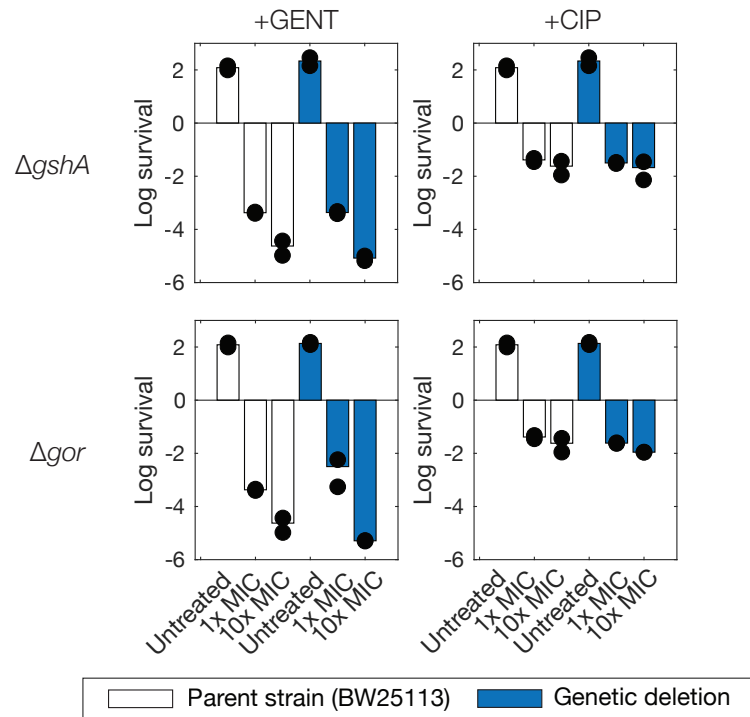
c, Survival of *E. coli* cells treated by kanamycin and ciprofloxacin (10x MIC) 6 h after treatment, as determined by CFU counting, corresponding to panel **b**. Positive values of the log survival indicate an increase in CFU/mL. Results are from two biological replicates (individual points), and bars indicate averages.



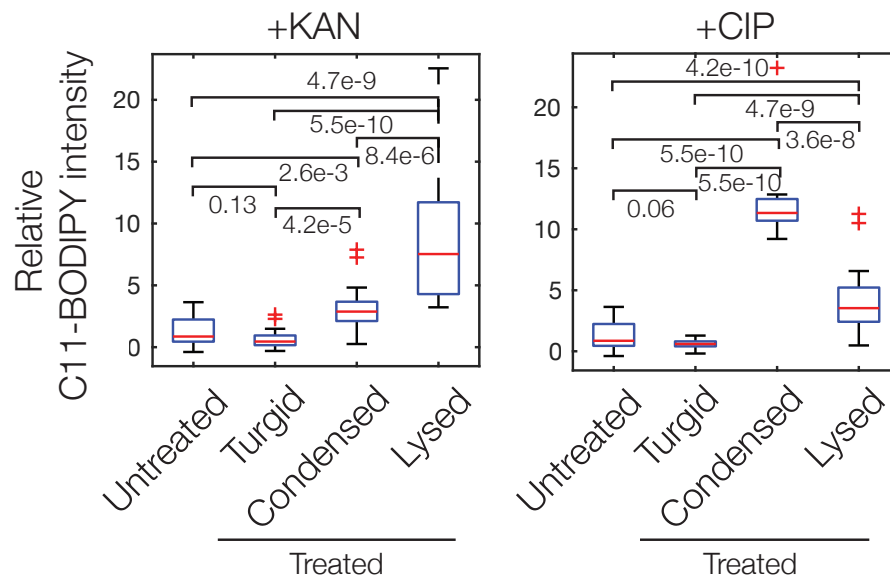
Supplementary Figure 12: **Bulk culture measurements of ATP abundance in cell cultures with and without glutathione pretreatment (10 mM)**. Cells were assayed in early log phase ($OD_{600} \approx 0.1$). For comparison, measurements for cells grown in LB diluted 1:1000 in PBS are shown. Error bars indicate one standard deviation, bars indicate averages, and data are presented as mean values \pm SEM. Individual measurements from biological replicates are shown as black points. Number of biological replicates in each condition: LB, 8; glutathione, 6; 1:1000 LB in PBS, 10.



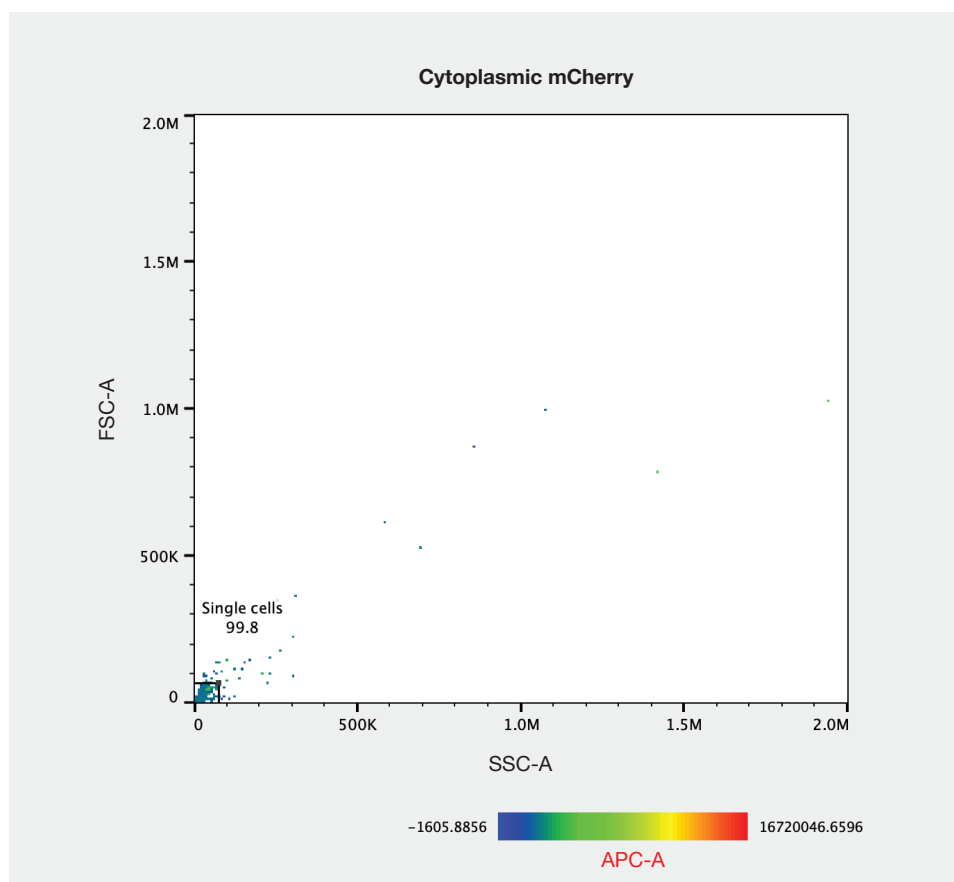
Supplementary Figure 13: **Measurements of lipopolysaccharide levels.** Shown are measurements of lipopolysaccharide (LPS) levels of bulk cultures of cells treated by antibiotics (10x MIC), as measured by an LAL assay. For comparison, data from treatment with 10x MIC ampicillin are included. Data from two biological replicates (black points), and bars indicate averages.



Supplementary Figure 14: **Effects of genetic deletions on antibiotic killing.** Shown are log survival values of *E. coli* under gentamicin and ciprofloxacin treatment, as determined by CFU plating and counting after 4 h of treatment. $\Delta gshA$ and Δgor strains from the Keio collection, as well as the parent strain (BW25113), were used. Data from two biological replicates (black points), and bars indicate averages. Positive values indicate increases in CFU/mL.



Supplementary Figure 15: **Measurements of C11-BODIPY fluorescence in the presence of α -tocopherol.** Shown are fluorescence intensities of antibiotic-treated *E. coli* pretreated by the lipophilic antioxidant α -tocopherol (50 mM), and in the presence of the lipid peroxidation-sensitive dye C11-BODIPY. The kanamycin and ciprofloxacin concentrations used were 10x MIC. Data are from 20 cells in each group. Box plots indicating the median (center), 25th percentile and 75th percentile (bounds of box), and extreme data points not considered outliers (bounds of whiskers) are shown, and red crosses indicate outliers including the minimum and maximum values. *p*-values for two-sample Kolmogorov-Smirnov tests are shown next to corresponding brackets.



Supplementary Figure 16: **Gating strategy for flow cytometry.** *E. coli* cells containing cytoplasmic mCherry were filtered by calibration of forward- and side-scattering area measurements (FSC-A and SSC-A) using the APC-A (red) fluorochrome. 20,000 scattering events are shown, and results are representative of four biological replicates with 20,000 scattering events each. The gating strategy was used for the flow cytometry measurements shown in Fig. 4 of the main text and Supplementary Figs. 1 and 8.

Supplementary References

1. Wong, F. & Amir, A. Mechanics and dynamics of bacterial cell lysis. *Biophys. J.* **116**, 2378–2389 (2019).
2. Dwyer, D. J. *et al.* Antibiotics induce redox-related physiological alterations as part of their lethality. *Proc. Natl. Acad. Sci. USA* **111**, E2100–E2109 (2014).
3. Yao, Z., Kahne, D. & Kishony, R. Distinct single-cell morphological dynamics under beta-lactam antibiotics. *Mol. Cell* **48**, 705–712 (2012).
4. Whatmore, A. M. & Reed, R. H. Determination of turgor pressure in *Bacillus subtilis*: a possible role for K⁺ in turgor regulation. *J. Gen. Microbiol.* **136**, 2521–2526 (1990).
5. Sun, Y., Sun, T.-L. & Huang, H. W. Physical properties of *Escherichia coli* spheroplast membranes. *Biophys. J.* **107**, 2082–2090 (2014).
6. Dougherty, T. J. & Saukkonen, J. J. Membrane permeability changes associated with DNA gyrase inhibitors in *Escherichia coli*. *Antimicrob. Agents Chemother.* **28**, 200–206 (1985).
7. Diver, J. M. & Wise, R. Morphological and biochemical changes in *Escherichia coli* after exposure to ciprofloxacin. *J. Antimicrob. Chemother.* **18**, 31–41 (1986).
8. Elliott, T. S., Shelton, A. & Greenwood, D. The response of *Escherichia coli* to ciprofloxacin and norfloxacin. *J. Med. Microbiol.* **23**, 83–88 (1987).
9. Wang, S., Arellano-Santoyo, H., Combs, P. A. & Shaevitz, J. W. Actin-like cytoskeleton filaments contribute to cell mechanics in bacteria. *Proc. Natl. Acad. Sci. USA* **107**, 9182–9185 (2010).
10. Koch, A. L. *Bacterial growth and form* (Springer Science & Business Media, 2001).
11. Hussain, S. *et al.* MreB filaments create rod shape by aligning along principal membrane curvature. *eLife* **7**, e32471 (2018).
12. Wang, S. & Wingreen, N. S. Cell shape can mediate the spatial organization of the bacterial cytoskeleton. *Biophys. J.* 541–552 (2013).
13. *et al.*, K. A. S. Protein diffusion in the periplasm of *e. coli* under osmotic stress. *Biophys. J.* 22–31 (2011).
14. Silhavy, T. J., Kahne, D. & Walker, S. The bacterial cell envelope. *Cold Spring Harb. Perspect. Biol.* **2**, a000414 (2010).
15. Movva, N. R., Nakamura, K. & Inouye, M. Regulatory region of the gene for the ompA protein, a major outer membrane protein of *Escherichia coli*. *Proc. Natl. Acad. Sci. USA* **77**, 3845–3849 (1980).
16. Cussler, E. L. *Diffusion: Mass Transfer in Fluid Systems* (Cambridge University Press, 1997).
17. Sperelakis, N. *Cell Physiology Source Book: Essentials of Membrane Biophysics* (Academic Press, 1995).
18. Phillips, R., Kondev, J., Theriot, J. & Garcia, H. *Physical Biology of the Cell* (Taylor and Francis, 2012).
19. Çetiner, U. *et al.* Tension-activated channels in the mechanism of osmotic fitness in *Pseudomonas aeruginosa*. *J. Gen. Physiol.* **149**, 595–609 (2017).
20. Deng, Y., Sun, M. & Shaevitz, J. W. Direct measurement of cell wall stress stiffening and turgor pressure in live bacterial cells. *Phys. Rev. Lett.* **107**, 158101 (2011).
21. Amir, A., Babaeipour, F., McIntosh, D. B., Nelson, D. R. & Jun, S. Bending forces plastically deform growing bacterial cell walls. *Proc. Natl. Acad. Sci. USA* **111**, 5778–5783 (2014).
22. Yao, X., Jericho, M., Pink, D. & Beveridge, T. Thickness and elasticity of Gram-negative murein sacculi measured by atomic force microscopy. *J. Bacteriol.* **181**, 6865–6875 (1999).
23. Cayley, D. S., Guttman, H. J. & Record, M. T. Biophysical characterization of changes in amounts and activity of *Escherichia coli* cell and compartment water and turgor pressure in response to osmotic stress. *Biophys. J.* **78**, 1748–1764 (2000).